Ductility of High-Burnup-Fuel ZIRLO™ following Drying and Storage

Spent Fuel and Waste Disposition

Prepared for
US Department of Energy
Spent Fuel and Waste Science and Technology

Argonne National Laboratory
M.C. Billone

June 30, 2019 Rev. 3
M2SF-19AN010201011
ANL-19/14

DISCLAIMER

This information was prepared as an account of work sponsored by an agency of the U.S. Government. Neither the U.S. Government nor any agency thereof, nor any of their employees, makes any warranty, expressed or implied, or assumes any legal liability or responsibility for the accuracy, completeness, or usefulness, of any information, apparatus, product, or process disclosed, or represents that its use would not infringe privately owned rights. References herein to any specific commercial product, process, or service by trade name, trade mark, manufacturer, or otherwise, does not necessarily constitute or imply its endorsement, recommendation, or favoring by the U.S. Government or any agency thereof. The views and opinions of authors expressed herein do not necessarily state or reflect those of the U.S. Government or any agency thereof.

SUMMARY

This report satisfies SFWD-SFWST-2019 milestone M2F-19AN010201011.

Previous results for ZIRLO™ (now ZIRLO®) cladding from high-burnup (HBU) fuel rods suggest that the ductility transition temperature (DTT) is highly sensitive to the peak cladding hoop stress in the range of 90±3 MPa following slow cooling under decreasing stress from peak cladding temperatures (PCTs) of 400°C and 350°C. In particular, the DTT was <30°C for peak cladding hoop stresses of 88±1 MPa and ≥125°C for peak cladding hoop stresses of 93 MPa and 94 MPa. However, the hydrogen content was lower (390−530 wppm) for the lower stresses and higher (560−650 wppm) for the higher stresses. In order to confirm this narrow stress dependence, two additional tests are required with radial hydride treatment (RHT) at 350°C PCT: (a) ≈350-wppm ZIRLO™ subjected to ≈94-MPa hoop stress at the PCT prior to cooling at 5°C/h and (b) ≈650-wppm ZIRLO™ subjected to ≈87-MPa hoop stress at the PCT prior to cooling at 5°C/h. Test (a) has been completed with a ZIRLO™ sample containing 350±70 wppm hydrogen and subjected to 95-MPa hoop stress at 350°C.

Prior to conducting the new test with ZIRLO™ rodlet 646B, criteria for ductility determination were evaluated and expanded. The initial criteria for determining the unloading point along the load-displacement curve were: (a) for highly brittle rings, which exhibit a load drop during elastic loading, a decrease in reloading slope (relative to the initial loading slope) of >50% indicates cracking through >50% of the cladding wall; this behavior was observed early in the program for high peak RHT hoop stresses and results were confirmed through experimental observations and finite element analysis; and (b) for rings that exhibit steep load drops >25% after initiation of plastic displacement, cracking is >50% of the cladding wall (based on metallographic examinations). In re-examining all previous load-displacement curves, it was observed that rings exhibiting minor load drops during the elastic-to-elastic/plastic displacement transition never achieved the expected loads exhibited by companion rings that cracked at larger displacements or by rings tested at higher temperature that did not crack. As a significant abrupt load drop is not observed in these cases, an “implicit” load-drop criterion was developed based on the percentage difference (>25%) between the anticipated load and the actual load achieved by the cracked ring. All previously generated load-displacement curves were re-evaluated using these three criteria to determine ring ductility. Ductility values for several important tests were reduced based on the implicit load-drop criterion.

The 646B ZIRLO™ rodlet containing 350±70 wppm was subjected to peak RHT conditions of 350°C and 95-MPa hoop stress for one hour and cooled at the controlled rate of 5°C/h down to 130°C followed by faster-slower natural cooling to room temperature. A mid-span ring (6-mm long) was sectioned for metallographic examination (MET) and five rings (8.0±0.3-mm long) were sectioned for ring compression testing. The outer-surface oxide layer thickness (27±1 μm) and cladding wall thickness (554±3 μm) were measured based on images at 12 locations around the cladding wall. These values, along with the cladding outer diameter (9.50 mm), were comparable to measurements for adjacent 80-mm-long segments 646C and 646D. The MET surface was etched to image (100X) the hydrides at about 40 circumferential locations covering the whole cladding surface. Higher-magnification (200X) images were also taken to confirm the continuity of the longest radial hydride in each of the 100X images. This procedure was repeated following regrinding/re-polishing/re-etching to image the surface about 0.1 mm from the first one examined. In terms of effective radial-hydride lengths, the maximum radial hydride length per 100X image was used to determine the radial hydride continuity factor (RHCF), which was 28±10% of the wall thickness with a maximum length of 53%. These results agree with expectations based on past data that the average and maximum RHCF would be about 30% and 50%, respectively.

Four of the rings were tested at 5-mm/s displacement rate and temperatures of 100°C, 120°C, 150°C, and 170°C. As expected, the rings tested at 100°C and 120°C were brittle (offset strains of 1.4±1.0% and 0.9%, respectively) and the ring tested at 150°C was ductile (3.5% offset strain). The sample tested at 170°C, which was 15 mm from the top weld, was fully ductile (9.3% offset strain), but it remains to be confirmed by MET that the RHCF in this region is in the range of 25% to 30%. Factors that could affect the relevance of this test are the axial extent of the discontinuity region along which the hoop stress increases from 0 MPa at the weld to 95 MPa and the length of the heat-affected zone (HAZ). As this end required only two turns (one attempt) of the weld-head electrode to get a good weld, the high-ductility results are not likely due to HAZ-induced annealing. The relevance of the 170°C test results is important in determining the DTT, which generally requires two brittle data points and two ductile data points.

The last test was conducted at 100°C and 0.05 mm/s displacement. It was an end ring adjacent to the ring tested at the same temperature. As the 100°C/(5-mm/s) load displacement curve was difficult to interpret, the purpose of the test was to stop the loading after the first small load drop at 0.4% offset strain and determine the extent of cracking. However, no load drops were observed and the sample was fully ductile (10%). Because it required 20 turns (10 attempts) to get a leak-proof weld, it appears as if the HAZ extended into at least part of this ring. In addition, the bottom end fixture has a 10-mm-long solid insert, as compared to the hollow top insert, which may result in an extension of the HAZ. MET will be used to study the axial profile of the RHCF to determine if hoop-stress reduction also occurred over part of the ring length during RHT. The results of these investigations are important for determining the distance the RCT ring has to be from the weld joint so that full irradiation hardening is retained and the whole length of the ring is subjected to the maximum hoop stress. The recommendation will be included in the ASTM guidance document being prepared for conducting radial hydride treatment and ring compression tests.

CONTENTS

FIGURES

TABLES

Page intentionally blank

REVISION HISTORY

Date	Revision	Changes
4/14/2019	0	Initial submission
4/20/2019	1	Editing
5/15/2019	2	Addition (Page 40) based on K. Sorenson's review comments
6/30/2019	3	Corrections based on J. Kessler review comments; final version

Page intentionally blank

ACRONYMS, UNITS AND SYMBOLS

ACRONYMS

AF	as-fabricated
ANL	Argonne National Laboratory
CWSRA	cold-worked, stress-relief annealed
DOE	U.S. Department of Energy
DTT	ductility transition temperature
EPRI	Electric Power Research Institute
FEA	finite element analysis
HAZ	heat-affected zone
HBU	high burnup
ISG	Interim Staff Guidance
NRC	Nuclear Regulatory Commission
OD	outer diameter
PCMI	pellet-cladding mechanical interaction
PCT	peak cladding temperature
PIE	post-irradiation examinations
PNNL	Pacific Northwest National Laboratory
PWR	pressurized water reactor
RCT	ring compression test
RHCF	radial hydride continuity factor (%)
RHT	radial-hydride treatment
RT	room temperature
RXA	recrystallized-annealed
SFWST	Spent Fuel Waste and Science Technology
TIG	tungsten inert gas (welding)
TMT	thermal-mechanical treatment
Zry-2	Zircaloy-2
Zry-4	Zircaloy-4

UNITS

°C	degree Celsius
GWd/MTU	giga-watt-days per metric tonne of uranium
h	hour
K	degree Kelvin
kN	kilo-newton
m	meter
mm	millimeter
µm	micro meter (micron)
MPa	mega-pascal
N	newton
s	second
wppm	weight parts per million

SYMBOLS

C_H	total hydrogen content in weight parts per million (wppm)
C_{HD}	dissolved hydrogen content at temperature T_D during heating (wppm)
C_{HP}	dissolved hydrogen content (wppm) needed to initiate hydride precipitation during cooling at temperature T_P
D_{mi}	inner diameter of cladding alloy (mm)
D_{mo}	outer diameter of cladding alloy (mm)
D_o	cladding outer diameter (includes outer-surface oxide layer if present, mm)
d_p	permanent displacement (pre-test minus post-test diameter in loading direction, mm)
d_p/D_{mo}	permanent strain (%)
δ	controlled sample displacement (mm) at the 12 o'clock sample position
δ_e	elastic displacement (mm)
δ_{max}	maximum sample displacement (mm) at the 12 o'clock sample position
Δp	pressure difference across cladding wall ($p_i - p_o$, MPa)
δ_p	corrected offset displacement (mm)
δ_{pt}	traditional offset displacement (mm)
δ_p/D_{mo}	corrected offset strain (%)
δ_{pt}/D_{mo}	traditional offset strain (%)
ΔT	temperature drop per drying cycle (°C)
ΔT_{PD}	difference between hydride precipitation (T_P) and dissolution (T_D) temperatures (°C)
E	Young's modulus (GPa)
$(\varepsilon_\theta)_{max}$	maximum hoop strain
h_m	cladding alloy wall thickness (mm)
h_{ox}	thickness of outer surface oxide layer (µm)
K_{LC}	calculated loading slope (i.e., loading stiffness) for RCT samples (kN/mm)
K_{LM}	measured linearized loading slope (kN/mm)
K_U	calculated linearized unloading slope (kN/mm)
K_{UM}	measured linearized unloading slope (kN/mm)
L	length of RCT sample (mm)
M_{max}	maximum RCT bending moment (N•m)
v	Poisson's ratio
P	measured RCT load at the 12 o'clock sample position
P_e	load during elastic displacement (N)
p_i	internal gas pressure (MPa)
P_{max}	maximum RCT load (N)
p_o	external gas pressure
R_{mi}	inner radius of cladding alloy (mm)
R_{mid}	mid-wall radius of cladding alloy (mm)
σ_θ	hoop stress (MPa)
T	temperature (°C)
T_D	hydrogen dissolution temperature (°C)
T_P	hydrogen precipitation temperature (°C)

1. INTRODUCTION

Structural analyses of high-burnup (HBU) fuel rods require cladding mechanical properties and failure limits to assess fuel behavior during long-term dry-cask storage, post-storage retrieval and transportation, and post-transport retrieval. License applications for transport casks containing HBU fuel assemblies with Zircaloy-2 (Zry-2), Zircaloy-4 (Zry-4) and ZIRLO® cladding have used properties and failure limits for as-irradiated cladding [1,2]. Reliable mechanical properties are not currently available for irradiated M5® cladding. The mechanical properties for irradiated M5® cladding will be measured by Pacific Northwest National Laboratory (PNNL) and Oak Ridge National Laboratory (ORNL) in the sister-rod test program (see Section 6). These properties will also be measured for fuel rods (ORNL) or defueled cladding segments (PNNL) that have been subjected to drying and storage peak hoop stresses at 400°C followed by ≤5°C/h controlled cooling. Pre-storage drying-transfer operations and early stage storage subject cladding to higher tensile hoop stresses induced by higher temperatures and internal pressures relative to in-reactor operation and pool storage. Under these conditions, radial hydrides may precipitate during slow cooling and may introduce an embrittlement mechanism if the cladding temperature decreases below a critical point, which is defined in this work as the ductility transition temperature (DTT). If embrittlement is predicted to occur within a temperature range relevant to transportation, then failure hoop stresses and strains would have to be revised to account for this effect.

In Interim Staff Guidance-11, Revision 3 (ISG-11, Rev. 3), the Nuclear Regulatory Commission (NRC) recommends a peak cladding temperature (PCT) limit of 400°C for high-burnup (≥45 GWd/MTU) fuel under normal conditions of storage and short-term loading operations (e.g., drying, backfilling with inert gas, and transferring the canister or cask to the storage pad) [3]. During loading operations, repeated thermal cycling (repeated heat-up/cool-down cycles) may occur but should be limited to fewer than 10 cycles, with cladding temperature variations (ΔT) that are less than 65°C per cycle, according to ISG-11, Rev. 3 (see Fig. 1 for justification of ΔT <65°C per cycle). One concern for HBU-fuel cladding is the possible precipitation of radial hydrides, which could embrittle cladding in response to tensile hoop stresses caused by internal pressure loading and “pinch-type” loading during transport. Limits established in ISG-11, Rev. 3, relied on data available before 2002, which were primarily for low-burnup and non-irradiated/pre-hydrided Zry-4. NUREG-2224 [4], which has been released for public comment, is more up to date and more extensive in terms of supporting data and analyses. It maintains the recommendation of 400°C PCT for HBU fuel. This NUREG also postulates that gross failure (>1-mm-wide crack) will not occur if the PCT is ≤400°C and cladding stresses are below the 0.2% offset-strain yield stress. Excessive radial hydride precipitation can result in failure at hoop stresses below the yield stress if the loads are high enough to approach the yield stress and if the temperatures are below the DTT.

Argonne National Laboratory (ANL) has developed a test protocol for studying HBU-fuel cladding embrittlement that has been used to generate data for NRC. Experimentally, the protocol involves two steps: (a) radial-hydride treatment (RHT), during which HBU-fuel cladding is exposed to simulated drying-storage temperature and hoop stress conditions, including slow cooling with decreasing stress, followed by (b) ring compression testing, in which rings sectioned from RHT HBU-fuel cladding are compressed to determine strength and ductility as a function of test temperature. The ring compression test (RCT) is used primarily as a ductility screening test, and the RCT loading simulates the pinch-type loading on HBU-fuel cladding that occurs during normal conditions of cask transport and potential drop accidents. The protocol was used to generate DTT data for HBU-fuel ZIRLO™ and Zry-4 [5, 6] (both efforts sponsored by NRC) and HBU-fuel M5® (sponsored by the U.S. Department of Energy [DOE]) [7]. Under DOE-sponsorship, ANL has also generated baseline characterization data and data for the strength and ductility of as-irradiated HBU-fuel Zry-4, ZIRLO™, and M5®. These data are important not only for determining the potentially degrading effects of drying and early stage storage, but also for

serving as reference properties for future evaluations of the effects of drying and storage on these cladding alloys [8–10]. Reference 11 documents ANL data generated through September 30, 2013, including additional DOE-sponsored test results for HBU-fuel ZIRLO™ and M5® following cooling from 400°C and lower hoop stress levels (80 to 90 MPa). Reference 12 contains refined interpretations of previously generated data, as well as test results for HBU-fuel ZIRLO™ subjected to 3-cycle drying at 350°C PCT and 93-MPa peak hoop stress. The decrease from 400°C to 350°C was a programmatic decision based on improved heat transfer models and decay heat rates indicating that it was highly unlikely that the PCT would exceed 350°C for current cask designs and fuel loading. Reference 13 contains additional data for as-irradiated HBU-fuel Zry-4 and for HBU-fuel ZIRLO™ following 1-cycle drying at 350°C PCT and 94-MPa peak hoop stress. Reference 14 presents results generated for HBU-fuel ZIRLO™ and M5® following RHT at 350°C and peak stresses in the range of 87-89 MPa. In Reference 15, the issue of continuity of radial hydrides in the axial direction is addressed. Past test results for HBU-fuel ZIRLO™ are summarized in Ref. 16, which also contains new data for as-irradiated ZIRLO™ with low (≈350 wppm) and high (≈650 wppm) hydrogen contents.

ANL test results indicate that susceptibility to radial-hydride precipitation during cooling is dependent on cladding alloy, thermal-mechanical treatment (TMT), total hydrogen content (C_H), C_H below the hydride rim, and peak RHT temperature and hoop stress. The combination of recrystallized-annealed (RXA) microstructure and low C_H results in higher susceptibility of M5® to precipitation of long radial hydrides during cooling. For cold-worked, stress-relief-annealed (CWSRA) alloys, ZIRLO™ was found to be more susceptible to radial-hydride precipitation than Zry-4. The differences in the distribution of hydrides across the cladding wall (lower for ZIRLO™ below the hydride rim) may be partly responsible for this behavior [6].

Section 2 of this report describes the ZIRLO™ materials and test methods used in this program. It has been updated to include changes in end-cap design, lower temperature (130°C vs. 200°C) for which 5°C/h cooling is maintained, and an improved formula for calculating the elastic stiffness of a ring. A generalized equation for calculating elastic stiffness as a function of the ratio of ring length to wall thickness is given in Section 3 based on new finite element analysis (FEA) calculations. Also presented in Section 3 are the FEA-calculated distributions of hoop stress in the ring for a small elastic displacement and a larger displacement into the elastic-plastic deformation regime. Data trends are presented in Section 4 for HBU-fuel ZIRLO™. In particular, ductility vs. test temperature data are separated into conditions leading to relatively high, medium and low ductility [17]. These results suggest a high-sensitivity of the DTT for this alloy to a narrow range of peak hoop stress (90±3 MPa) for which the DTT increases from <30°C to ≥125°C.

New ductility results for HBU-fuel ZIRLO™ with 350 wppm C_H are presented in Section 5. Prior to conducting RCTs, the rodlet was subjected to peak RHT conditions of 350°C and 95 MPa and cooling at 5°C/h down to 130°C. The expectations from previous results are (a) the effective radial hydride length averaged over the cladding cross section would be about 30±3% of the cladding wall thickness, (b) the longest radial hydride would be ≈50% of the cladding wall, and (c) the DTT would be >120°C. The new test results were in excellent agreement with expectations based on data trends.

To appreciate the influence of PCT (i.e., decrease from 400°C to 350°C), stress, temperature cycling, and hydrogen content on radial hydride precipitation and embrittlement, it is important to summarize literature results for hydrogen dissolution and hydride precipitation. Unlike most, if not all, studies of radial hydride precipitation and subsequent ductility, the ANL RHT process includes decreasing internal gas pressure and hoop stress with decreasing temperature during cooling, as would occur in fuel rods during storage. Most researchers have used an actively pressurized cladding tube for which the pressure

is kept constant during cooling. As such, it is important to understand the dependence of hydrogen solubility (C_{HD}) on temperature (T_D) during the heating phase and the content of dissolved hydrogen (C_{HP}) needed to initiate precipitation of new hydrides at the precipitation temperature (T_P) during the cooling phase. Figure 1 summarizes the data of Kearns [18], Kammenzind et al. [19], and McMinn et al. [20] for these parameters, as well as the temperature gap (ΔT_{PD}) between precipitation and dissolution. As shown in Fig. 1, the solubility of hydrogen at 400˚C is 206±5 wppm and the precipitation temperature for new hydrides is 335˚C. The hydrogen solubility at 350˚C is 126±6 wppm and the precipitation temperature for new hydrides is 285°C. These results are applicable to the HBU-fuel Zry-4 and ZIRLO™ samples used in the ANL test program because these samples contained ≥300 wppm for Zry-4 and ≥350 wppm for ZIRLO™. However, the HBU-fuel M5® samples tested by ANL contained lower hydrogen content (58−94 wppm) for which total dissolution occurred during the heating ramp at temperatures in the range of 290−330°C. Corresponding temperatures at which precipitation initiated were in the low range of 225−265˚C. In addition, it has been shown that dissolution and precipitation temperatures for Nb-containing alloys (Zr-1Nb alloy M5® and Zr-1Sn-0.26Nb alloy N18) were essentially the same as those measured for Zry-4 [21]. These results suggest that the data in Fig. 1 also apply to ZIRLO™. More significant than differences in alloy composition, thermal-mechanical treatment (i.e., level of cold work) and fast-neutron damage levels are the differences in T_D and T_P measured from diffusion couples [18, 19] and those measured using differential scanning calorimetry [20, 21]. In the current work, the diffusion-couple data from long-time tests at temperature are used because they appear to be more applicable to drying and storage time duration (see Section 6 for discussion on how to use Fig. 1).

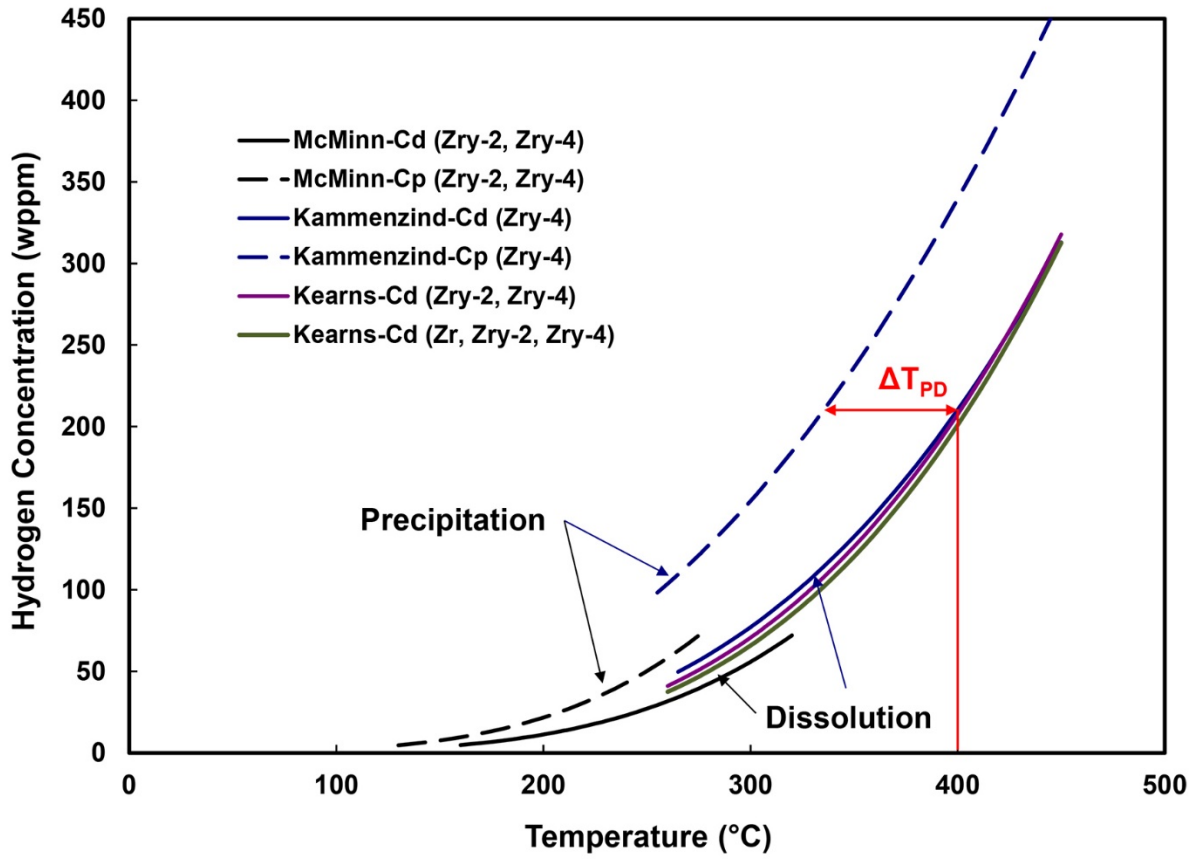

Figure 1: Steady-state curves for hydrogen dissolution and precipitation in Zr alloys.

Page intentionally blank

2. HBU-FUEL CLADDING MATERIALS AND TEST METHODS

2.1 HBU-FUEL CLADDING MATERIALS

Table 1 lists the HBU-fuel ZIRLO™ (now ZIRLO®) samples referred to in this report. The new FY2019 test material is listed in bold font. For rodlets subjected to three drying cycles, the hold time at PCT refers to the hold time per cycle. The materials came from fuel rods irradiated in the same assembly to HBU (68±2 GWd/MTU) in the North Anna pressurized water reactors (PWRs). The $\pm C_H$ values represent one standard deviation in data collected from multiple axial locations along each segment and quarter-ring samples at each axial location. The large one-sigma values were due to circumferential variation in C_H, especially for average C_H values >350 wppm. These variations are much larger than the circumferential variation in outer-surface oxide layer thickness (h_{ox}). Additional characterization results are presented in subsequent sections. σ_θ is the average hoop stress across the cladding wall at the PCT.

Table 1 Summary of HBU-fuel ZIRLO™ cladding materials used in studies of cladding ductility for as-irradiated cladding and following simulated drying and storage RHT at PCT.

ANL ID	Burnup, GWd/MTU	h_{ox}, µm	C_H, wppm	σ_θ(PCT), MPa	PCT, °C	Hold Time, h (cycles)
646C	66	30±1	≈390±70	<70	350	24 (1)
105A	68	47±11	530±70	—	—	—
105B	68	48±3	535±50	80	400	1 (1)
105G	68	59±1	≈350	—	—	—
646D	66	30±1	387±72	87	350	24 (1)
105D	68	40±5	480±131	88	400	1 (3)
105C	68	47±3	530±115	89	400	1 (1)
105E	68	48±6	564±177	93	350	1 (3)
105F	58	58±3	644±172	94	350	1 (1)
646B	**66**	**27±1**	**350±70**	**95**	**350**	**1 (1)**
648C	70	26±2	348±80	111	400	24 (1)
648D	70	33±3	425±63	111	400	1 (1)
648G	70	52±7	654±193	141	400	1 (1)

The three fuel rods were irradiated for four 18-month cycles. Cycles 1, 2, and 4 were irradiated at relatively high linear heat rating. Irradiation for the 4th cycle, which occurs for lead-test-assembly fuel rods, is atypical as is the relatively high linear heat rating for this cycle. Such irradiation conditions result in a high temperature gradient across the cladding wall and a rather dense, localized hydride rim just below the oxide/cladding interface with relatively few circumferential hydrides below this rim. Figure 2 shows the hydride distribution across the cladding wall for a sample with 318±30 wppm (adjacent ring to surface shown in the figure). Most of the hydrogen is concentrated in the hydride rim with a few dominant circumferential hydrides closer to the mid-radius. Figure 3 shows the surface at an orientation 180° from the image shown in Fig.2. The distribution of the circumferential hydrides is similar at both orientations, but radial hydrides are observed near the cladding inner surface. These radial hydrides likely occurred during reactor-shutdown cooling due to localized pellet-clad mechanical interaction (PCMI). The hydride distribution shown in Figs. 2−3 is similar to what is observed at higher hydrogen contents. Figures 4−5 show the hydride distribution for a cladding surface at a higher elevation of the same fuel rod for which the average C_H is about 660 wppm.

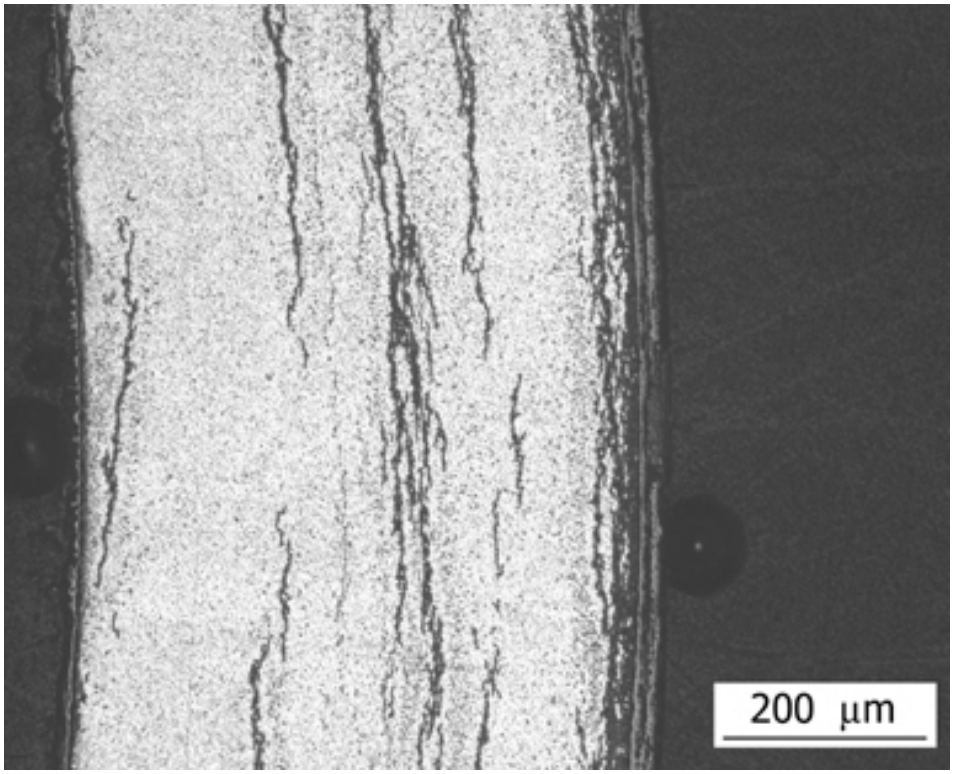

Figure 2: HBU-fuel ZIRLO™ surface with 318±30 wppm C_H at the 3 o'clock orientation.

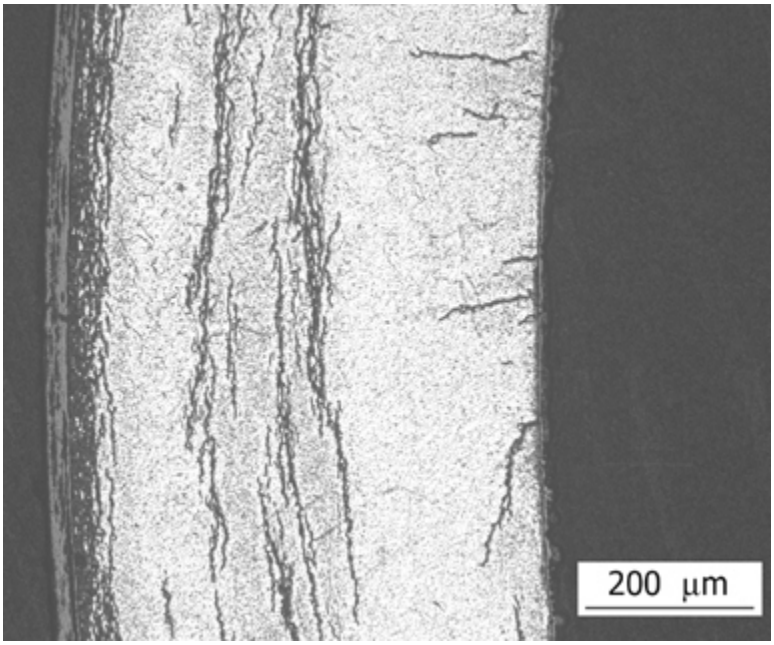

Figure 3: HBU-fuel ZIRLO™ surface with 318±30 wppm C_H at the 9 o'clock orientation.

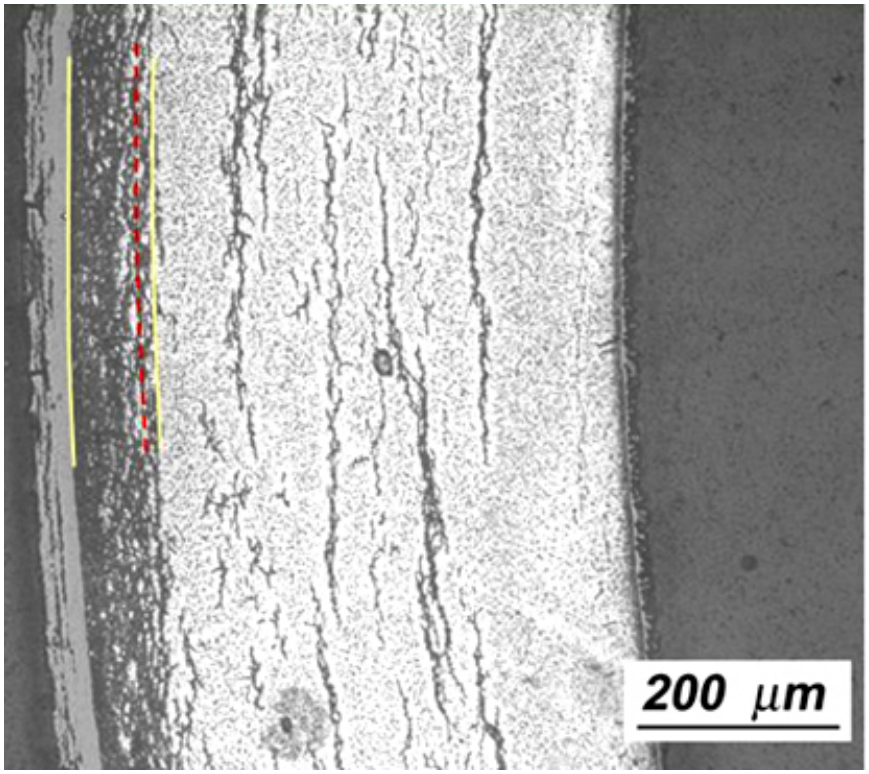

Figure 4: HBU-fuel ZIRLO™ surface with 657±148 wppm C_H and maximum hydride rim thickness.

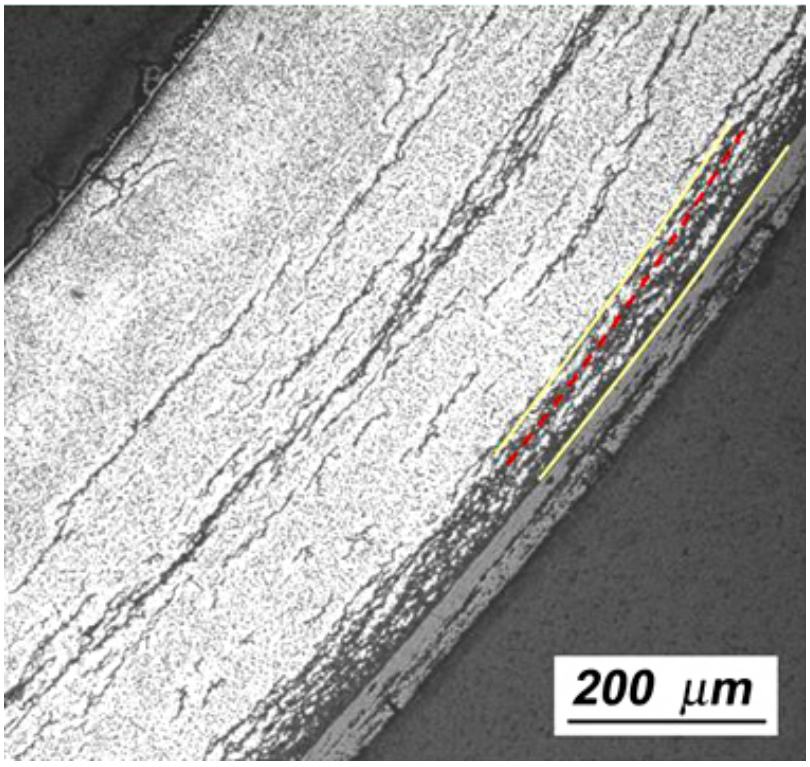

Figure 5: HBU-fuel ZIRLO™ surface with 657±148 wppm C_H and minimum hydride rim thickness.

The thin ring adjacent to this surface contained 657±148 wppm C_H. The primary difference between the low C_H images (Figs. 2-3) and the high C_H images (Figs. 4-5) is the thickness of the hydride rim. For the high C_H sample, the rim thickness varied systematically from about 40 µm to 70 µm, which accounts for the large circumferential variation in C_H measured for four quarter rings adjacent to the images. The circumferential variation in C_H is likely due to small circumferential variations in cladding temperature due to asymmetric heating and cooling from the presence of assembly edges and corners and from the presence of guide and instrumentation tubes. Samples with intermediate hydrogen contents (350 wppm to 650 wppm) showed similar distributions of circumferential hydrides. For the baseline ZIRLO™ studies, segment 105A in Table 1, C_H data for one ring indicated the presence of 515±70 wppm hydrogen. Following removal of the outer-surface oxide layer and about a third of the cladding outer wall, the hydrogen content dropped to 136±7 wppm. The hydride distribution in these high-power fuel rods tends to lead to higher ductility in as-irradiated cladding and longer radial hydrides emanating from the cladding inner surface following RHT. If the RHT hoop stress is high enough, radial hydrides can grow up to 50% of the cladding wall before encountering a circumferential hydride. Thus, the ZIRLO™ tested in the ANL program, should be more susceptible to the precipitation of long radial hydrides within the inner region of the cladding wall than lower-power fuel rods with a more diffuse distribution of circumferential hydrides in the as-irradiation condition.

2.2 TEST METHODS

The protocol for single-cycle heating-cooling tests consisted of two steps: (a) simulated drying and storage testing RHT during which a sealed, pressurized rodlet is heated to and stabilized at the PCT within one hour, held at the PCT for 1−24 hours, cooled slowly (by laboratory standards) at 5°C/h to 200°C (≈130°C for low-C_H M5®), and cooled at a higher rate to room temperature (RT) and (b) ring-compression testing at three to four temperatures from RT to 200°C and at 5 mm/s (reference value) displacement rate to a maximum sample displacement (δ_{max}) of 1.7 mm. For three-cycle heating-cooling RHTs, rodlets were heated to the PCT, held at PCT for one hour, cooled at 5°C/h to 100°C below the PCT, and reheated to the PCT for each cycle. For the last four ZIRLO™ rodlets (105F, 646D, 646C and 646B) with 350°C PCT, the 5°C/h cooling rate was maintained down to 130°C to give the dissolved hydrogen (≈125 wppm) more time to precipitate. The temperature history for these tests is shown in Fig. 6.

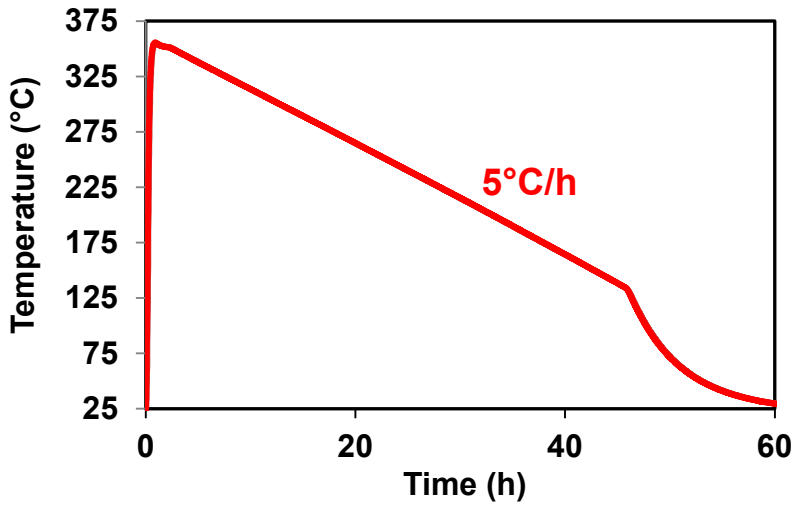

Figure 6: Rodlet RHT temperature history for controlled cooling from 350°C.

HBU-fuel cladding segments were used to fabricate the sealed and pressurized (with argon) rodlets. Following outer- and inner-surface oxide removal at the ends of the samples, as well as squaring of the ends, the components to be assembled are shown in Fig. 7. From left to right, these components include the solid bottom end fixture with a 15-mm insert, the zirconia pellet used to reduce gas volume and stored energy, the HBU-fuel cladding segment, and the hollow top end fixture with a 15-mm insert, which has a small hole at the top to allow for pressurization. In general, the fabrication sequence consists of circumferential welding of the bottom end plug, loading of the pellet, circumferential welding of the top end plug, pressurization in a chamber, laser-welding the top end-fixture hole with the rodlet in the chamber, and checking to ensure that the rodlet is indeed sealed and holds pressure. All previous rodlets (excluding the new 646B test) were fabricated from the components shown in Fig. 7

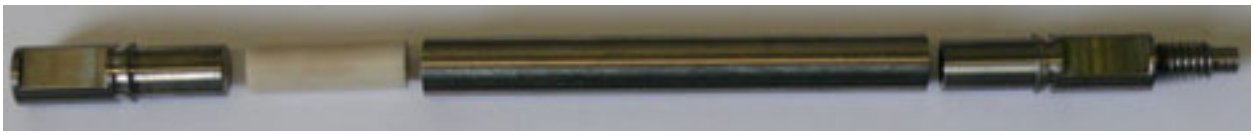

Figure 7: Rodlet bottom end fixture, zirconia pellet, cladding segment, and top end fixture.

Although performing the circumferential weld is the most difficult rodlet fabrication step, a successful weld depends on the quality of the oxide removal, especially removal of the inner-surface oxide layer. For the long end caps shown in Fig. 7, inner-surface oxide removal must extend about 15−19 mm from each end. Inner-surface oxide removal is performed by stationary reamers with the sample rotated in a mini-lathe. With such a crude setup, it is difficult to remove all the inner-surface oxide within the span needed without thinning the cladding wall at the ends. The end caps have been redesigned such that the length of the inserts has been reduced from 15 mm to 10 mm (see Fig. 8). This reduces the length of the heat-affected zone (HAZ). Further modifications are being considered, which include reducing the insert length to 5 mm and hollowing out the bottom solid insert to further decrease the HAZ. The main purpose of the insert is to stabilize the position of the end fixture relative to the end of the cladding segment. The primary weld occurs between the flange just above the insert and the cladding wall. The Astro Arc welder used for circumferential welding has an electrode that revolves around the joint to be welded. Welding is conducted in an argon chamber and the process is essentially tungsten-inert-gas (TIG) welding.

Figure 8: Rodlet bottom end fixture (redesigned), cladding segment, and top end fixture (redesigned).

Prior to rodlet pressurization, the outer diameter (OD) is measured for each cladding segment at two orientations (90° apart) and at three axial locations. These values are averaged to give the cladding outer diameter (D_o). The thickness of the outer-surface oxide layer (h_{ox}) is estimated from sibling-rod data or from interpolation or extrapolation of data from the same fuel rod at different axial locations.

The same approach is used to estimate the cladding-alloy wall thickness (h_m). The outer diameter of the cladding alloy (D_{mo}) is calculated from $D_o - 2\ h_{ox}$, and the cladding alloy inner diameter (D_{mi}) is calculated from $D_{mo} - 2\ h_m$. The ratio R_{mi}/h_m, where R_{mi} is the cladding alloy inner radius, is used in Eq. 1 to calculate the average hoop stress (σ_θ) from the pressure difference ($\Delta p = p_i - p_o$) across the cladding wall, where p_i and p_o (0.1 MPa during fabrication at 23°C and 0.17 MPa in the RHT furnace) are internal and external pressures, respectively.

$$\sigma_\theta = (R_{mi}/h_m)\ \Delta p - p_o \qquad (1)$$

The ideal gas law is used to relate p_i at the PCT to p_i at 23°C: $p_i(\text{PCT}) = ([\text{PCT} + 273\text{K}]/296\text{K})\ p_i(23°\text{C})$. Given the target σ_θ at the PCT, the fabrication pressure at 23°C can be calculated using Eq. 1.

Following RHT, the rodlet is depressurized and sectioned for C_H samples, RCT samples, and metallographic imaging samples, from which precise values of the geometrical parameters in Eq. 1 can be determined. Using this procedure, the calculated target peak rodlet σ_θ has been found to be within ±3 MPa of the actual value.

The second phase of the test protocol consists of RCTs. Figure 9 shows a schematic of RCT loading. The RCT load induces maximum hoop bending stresses (σ_θ) at the inner surfaces of the 12 (under load) and 6 (above support) o'clock positions. Tensile hoop stresses also occur at the 3 and 9 o'clock outer surfaces. Associated with these tensile stresses are tensile strains (ε_θ). Within the elastic range, hoop stresses at 3 and 9 o'clock are about 40% less than hoop stresses at 12 and 6 o'clock. Also, because the length (L ≈ 8 mm) of the rings is much greater than the cladding wall thickness (0.54 to 0.57 mm for HBU-fuel ZIRLO™ and M5®), an axial stress is induced that is up to 0.37 times the hoop stress within the elastic deformation regime. The maximum sample displacement (δ_{max} = 1.7 mm) is chosen to give ≈10% offset strain at RT. The starting point for the RCT is 1 mm above the sample to allow the full displacement rate to develop. The reference displacement rate is 5 mm/s.

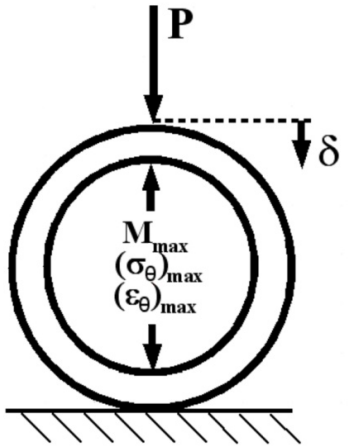

Figure 9: RCT measured load (P) and controlled displacement (δ).

Load-displacement curves and post-test diameter measurements are used to determine offset (δ_p) and permanent (d_p) displacements, respectively. These are normalized to D_{mo} to give relative plastic displacement (i.e., plastic strain) for the ring structure. Permanent displacement is defined as the difference between pre- and post-test diameter measurements along the loading direction. Figures 10

and 11 show how traditional (δ_{pt}) and corrected (δ_p) offset displacements are determined from benchmark load-displacement curves for as-fabricated (AF) 17×17 M5® rings subjected to displacements of 1.7-mm displacement (Fig. 10) and 0.5-mm (Fig. 11). For the benchmark samples, D_{mo} = 9.49 mm in the loading direction, h_m = 0.57 mm, and L = 8.06 mm. The traditional offset-displacement methodology calls for unloading the sample at the same slope as the measured linearized loading slope (K_{LM}). It should be noted that K_{LM} is less than the calculated sample stiffness (K_{LC}) due to the influence of machine compliance. For the case shown in Fig. 10, this approach gives a traditional δ_{pt} = 1.24 mm, which is greater than the more accurate d_p = 1.10 mm based on the difference between pre- and post-test diameters. Thus, there is an inherent error in the traditional approach as the measured linearized unloading slope (K_{UM}) is always less than K_{LM}. K_{UM} is determined from the slope of the line connecting δ_{max} to the displacement axis value based on the measured value of d_p at zero load. Normalizing these displacements to D_{mo} gives 13% traditional offset strain and 11.6% permanent strain, which is also the corrected offset strain (δ_p) for these benchmark tests. As noted in Fig. 10, K_{UM}/K_{LM} is 0.771. As the total and traditional offset displacements decrease, the difference between δ_{pt} and d_p decreases. This is shown in Fig. 11 for which δ_{pt} is 0.11 mm, d_p is 0.09 mm, and K_{UM}/K_{LM} is 0.944.

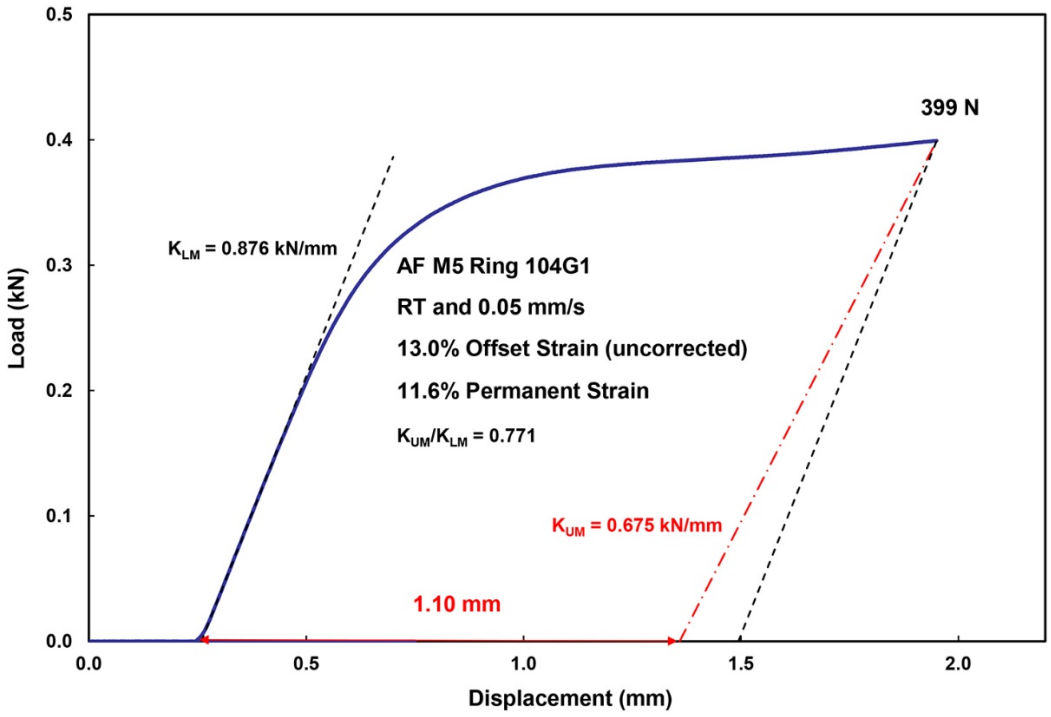

Figure 10: Load-displacement curve for as-fabricated (AF) M5® ring tested at RT and 0.05 mm/s to 1.7-mm ring displacement.

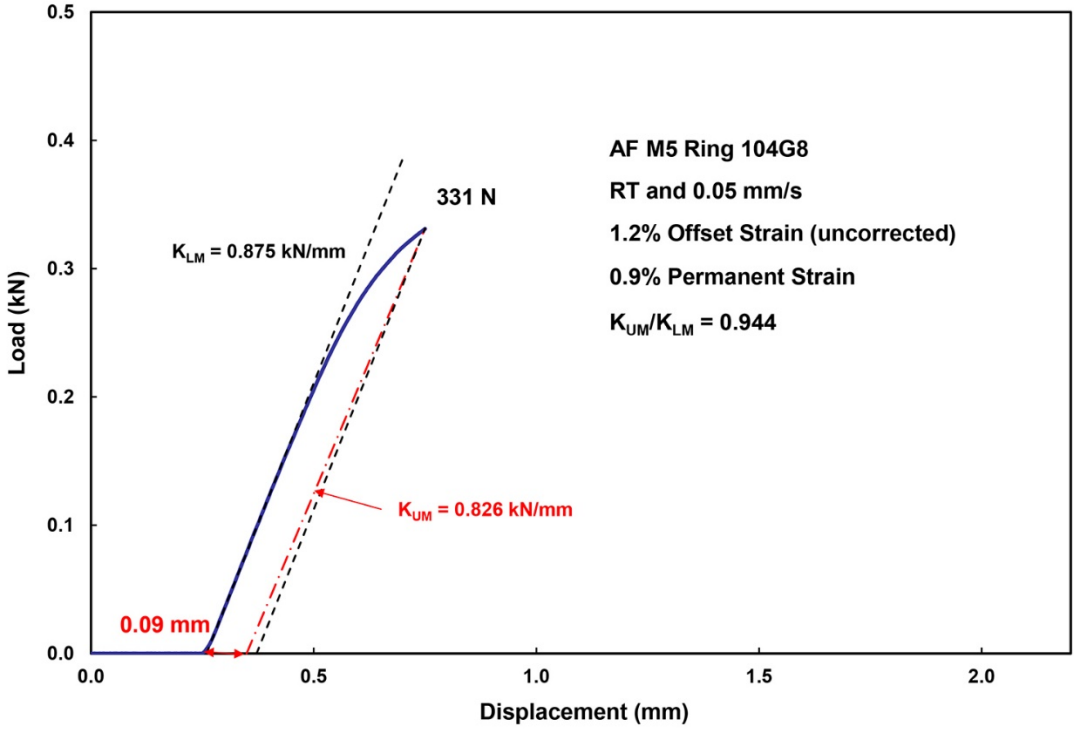

Figure 11: Load-displacement curve for AF M5® ring tested at RT and 0.05 mm/s to 0.5-mm ring displacement.

Energy methods were used to determine the bending moment as a function of circumferential orientation. Both wide-beam and narrow-beam assumptions were used to relate the bending moment to bending stresses and strains within the elastic-deformation regime, as well as the relationship between the elastic load (P_e) and elastic displacement (δ_e). The curvature of the ring was not taken into account in the bending analysis. The calculated loading stiffness is $K_{LC} = P_e/\delta_e$, where

$$P_e = f(v) \{(E\ L)/(1.79)\} (h_m/R_{mid})^3\ \delta_e \qquad (2)$$

In Eq. 2, E is Young's modulus (91.9 GPa for RXA alloys at room temperature [1]), v is Poisson's ratio (0.37 for RXA and CWSRA alloys at RT to 400°C [2]), and $R_{mid} = (D_{mo} - h_m)/2$ is the mid-wall radius. For a narrow beam (in terms of the length [L] to h_m ratio), f(v) = 1. For a wide beam ($L/h_m >> 1$), it is difficult for the material to expand or contract in the length direction and the assumption of zero strain in the length direction leads to $f(v) = 1/(1 - v^2) = 1.16$. However, no guidance is given in the literature for determining f(v) as a function of L/h_m. FEA calculations, which are described and discussed in Section 3, demonstrate that for L= 8 mm, f(v) = 1.09 for h_m = 0.57–0.61 mm (L/h_m = 13.1 to 14.0), which is close to half way between the narrow- and wide-beam solutions.

For HBU-fuel cladding rings that crack during the 1.7-mm displacement, d_p cannot be determined accurately. Thus, one must rely on a correlation for the unloading slope to determine the corrected offset displacement prior to the first significant crack, from which the ductility can be determined. The correlation developed for this application is based on the results from a large number of benchmark tests with permanent displacements ranging from 0.09 mm to 1.4 mm, displacement rates in the range of 0.03–50 mm/s, and temperatures in the range of 20–150°C. Results of these benchmark tests are

shown in Fig. 12 for the ratio of measured unloading/loading (K_{UM}/K_{LM}) slopes vs. traditional offset strain (δ_{pt}/D_{mo}). Also shown in Fig. 12 are results from nine RCTs with HBU-fuel M5® (solid red circles) that exhibited no cracking after 1.7-mm total displacement. The blue hollow-circle data points are from RCTs conducted with AF 17×17 M5® (48 points) and AF 17×17 ZIRLO™ (6 points) cladding samples. Outer diameters were 9.49±0.1 mm and nominal cladding wall thickness values were 0.61 mm (reference case) and 0.57 mm (6 ZIRLO™ data points and 15 M5® data points). The data set includes RCT results from two machines: (a) the screw-type Instron 5556 and (b) servo-hydraulic Instron 8511. Results are also shown for shorter (6 mm) and longer (10 mm) rings, as well as larger-diameter 15×15 M5® rings.

The correlation for the ratio K_U/K_{LM} and δ_{pt} (in %) is:

$$K_U/K_{LM} = 1 - 0.0303\ \delta_{pt}/D_{mo} \text{ for } \delta_{pt}/D_{mo} \leq 8.0\% \quad (3a)$$

$$K_U/K_{LM} = 0.758 \text{ for } \delta_{pt}/D_{mo} > 8.0\% \quad (3b)$$

The stiffness ratio for HBU-fuel M5® with >8% traditional offset strain is 0.746, which is in excellent agreement with the 0.758 determined for AF cladding materials.

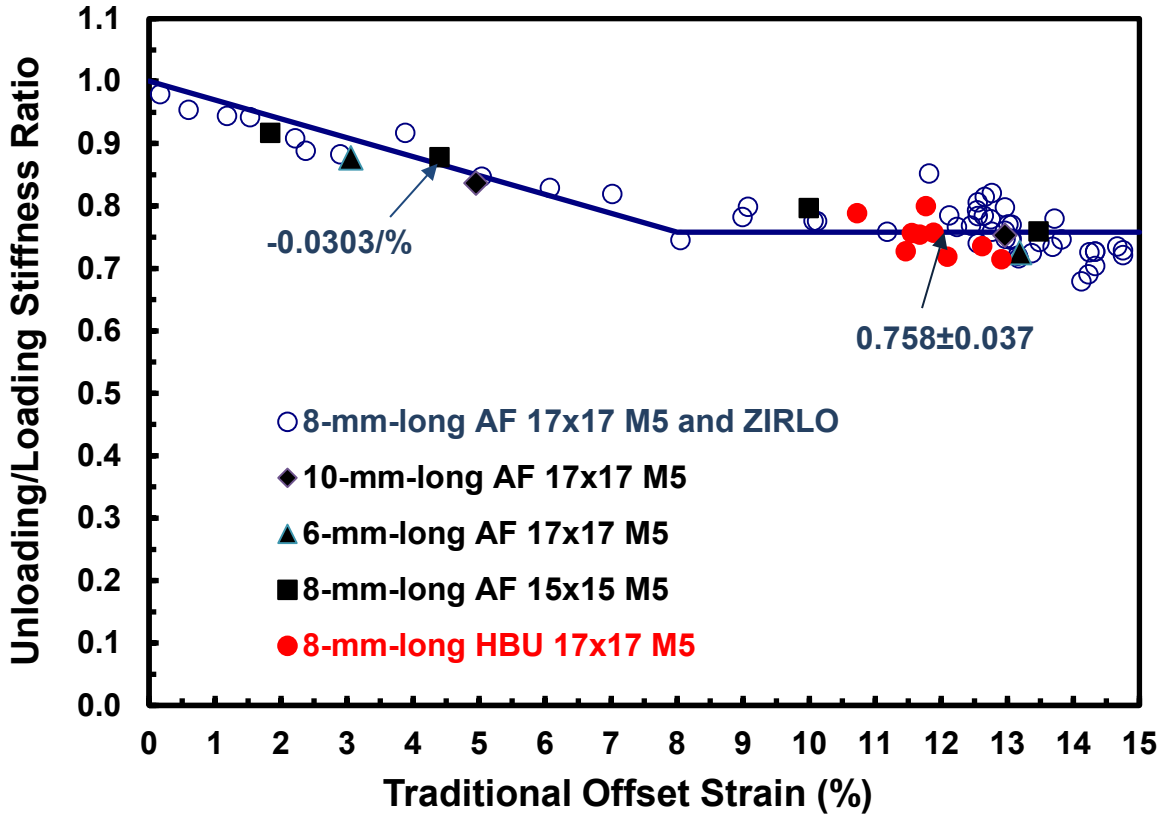

Figure 12: RCT benchmark results for determining the ratio of unloading/loading stiffness as a function of the traditional offset strain.

There is reasonable confidence in using Eqs. 3a and 3b to calculate the corrected offset displacement (δ_p) and corresponding corrected offset strain (δ_p/ D_{mo}) for cladding rings that do not exhibit a single wall crack <25% of the cladding wall or multiple shorter cracks prior to a significant load drop. However, with the possible exception of HBU-fuel M5® with long radial hydrides, sparsely distributed circumferential hydrides, and a thin oxide layer (≈10±3 μm), most HBU-fuel cladding samples exhibited some cracking prior to the maximum displacement or prior to a significant load drop. The effects of minor cracks (e.g., multiple short cracks through the hydride rim) can reduce the unloading slope by as much as 25%. A large number of tests with HBU-fuel cladding would be needed to develop a correlation for unloading slope as a function of number and depth of cracks. These tests would have to be conducted at a slow enough displacement rate (e.g., 0.05 mm/s) in order to terminate the test before major cracking had occurred. The compressed rings would then have to be subjected to metallographic examination to determine crack location, number, and depth. Until such tests are performed, uncertainty in the determination of the corrected offset strain has to be taken into account in the formulation of an embrittlement criterion. A set of criteria is described in the following.

Two of the criteria for determining embrittlement remain the same for cladding with radial and circumferential hydrides: δ_p/D_{mo} <2% prior to >25% load drop or >50% decrease in loading slope. In previous work [5–6], it was established that >25% load drop or >50% decrease in re-loading slope corresponds to a crack or cracks extending through >50% of the wall thickness. A third criterion was added within the past two years for load-displacement curves that indicated major cracking could occur within the transition from elastic to elastic-plastic displacement without exhibiting either a 25% load drop or a 50% decrease in elastic re-loading slope, for which an “implied” load drop >25% is used. Although such cases are relatively rare, the implied load drop criterion can result in a significant decrease in ductility. The implied load drop is illustrated in Figure 13 for a HBU-fuel M5® sample (80±7 wppm) from a rodlet subjected to peak RHT conditions of 350°C/89-MPa, which led to long radial hydrides (44±18% RHCF). The solid blue load-displacement curve is for a sample tested at 23°C. The dashed-line black curve is for the ring tested at 60°C. The 23°C load-displacement curve shows a series of minor load drops initiated during elastic loading. The reloading slope after the first load drop from 310 N to 262 N is too short to enable a reliable slope (stiffness) calculation. This is followed by two additional small load drops before the load increases smoothly with displacement. If severe cracking is assumed to occur during the first load drop, the sample would have an offset strain of only 0.3% and be considered brittle. If severe cracking were assumed to occur during the second load drop, the sample would appear to have an offset strain >2% and be considered ductile. However, the unloading slope from the peak of the second load drop would be much smaller than predicted by Eq. 3a due to cracking. Figure 14 shows that the sample had a through-wall crack at the 12 o’clock orientation. There was also a long crack at the 6 o’clock orientation. However, the 60°C ring achieved a peak load of 438 N prior to the 39% load drop, which resulted in an offset strain of only 1.6% (brittle). This was followed by a second severe load drop indicating at least two long cracks. It is evident that the 23°C ring was as severely cracked as the 60°C ring because they both had about the same load-carrying capacity beyond 1.2 mm on the displacement axis. It is clear from this comparison that severe cracking occurred during the first load drop for the 23°C ring even though the observed load drop was only 15%. The implied load drop is >25% and as much as 40% for this case.

The 2% offset strain limit is based on the uncertainty in the measurement of the permanent displacement (pre-test diameter minus post-test diameter, d_p) for HBU-fuel cladding and the added uncertainty in the permanent displacement measurement for HBU-fuel cladding due to flaking off of the oxide layer under the applied loading plate and above the support plate. Multiple cracks through the oxide layer and the hydride rim lower the unloading stiffness to values less than shown in Fig. 12, which has also been factored into the 2% offset-strain limit. An additional consideration is that the material

strain is less than the ring structural strain (i.e., permanent and corrected offset displacements normalized to the cladding outer diameter). The peak elastic strain in the material is about 0.3 times the structural strain. As the HBU-fuel M5® tested had very thin oxide layers (10±3 µm) and no hydride rim, the 2% offset strain criterion is more conservative for this HBU-fuel alloy than for the HBU-fuel Zry-4 and ZIRLO™ samples tested, both of which had thicker oxide layers (30−100 µm) and thick hydride rims (30−100 µm).

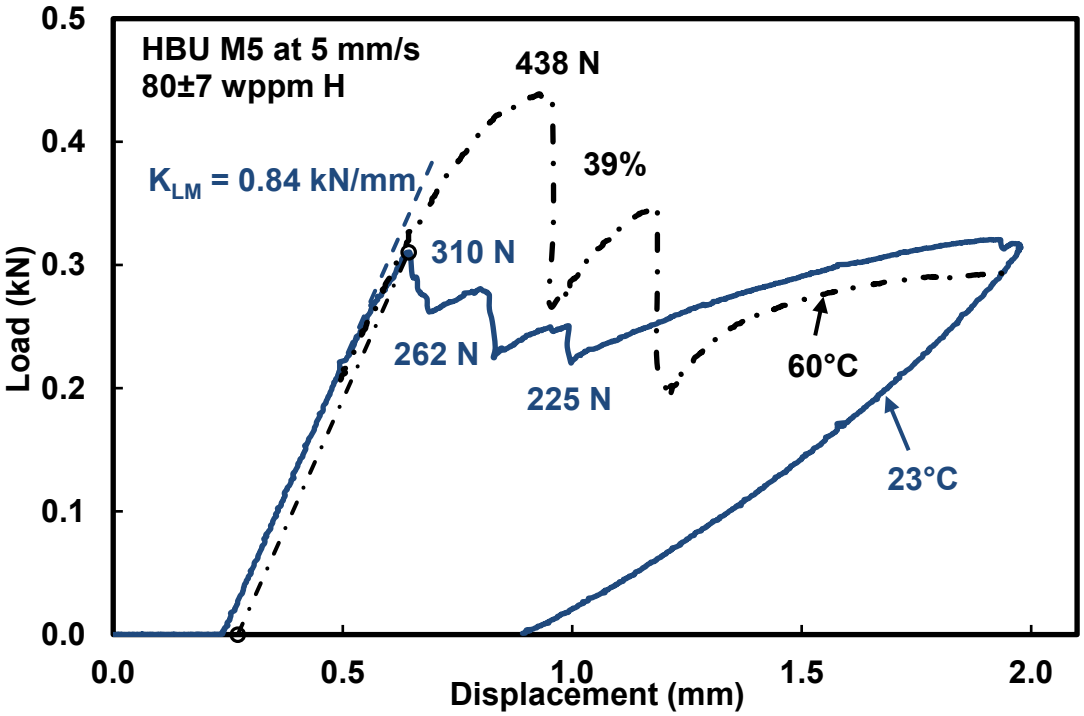

Figure 13: Load-displacement curves for HBU-fuel M5® with 80±7 wppm C_H following RHT at peak conditions of 350°C/89-MPa.

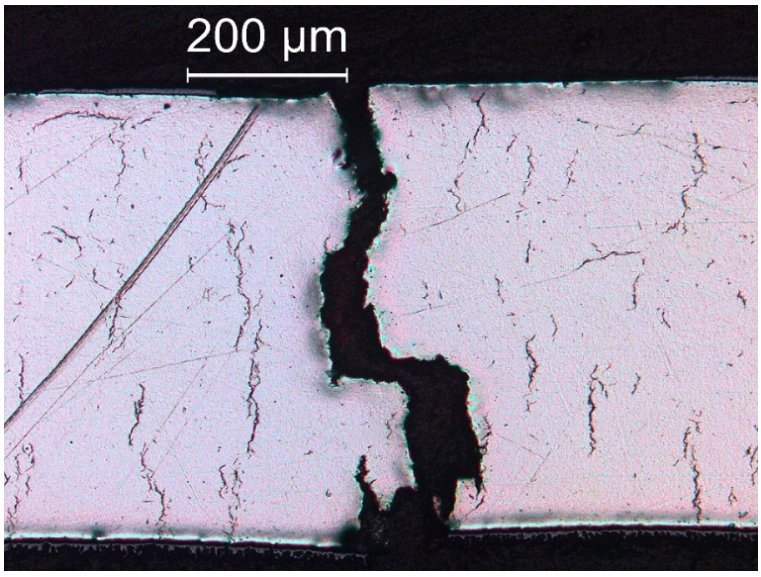

Figure 14: Through-wall crack in HBU-fuel M5® ring tested at 23°C following 350°C/89-MPa RHT.

Page intentionally blank

3. FEA RESULTS FOR RCT SAMPLES

The FEA model was developed using ABAQUS for cladding rings subjected to RCT loading. The model includes the machine stiffness (>10 kN/mm), elastic properties for M5® (e.g., E= 91.9 GPa and ν = 0.37 at RT), large strain capability and anisotropic plastic stress-strain properties. Literature values [22] for the hoop tensile properties of AF M5® were based on results of ring-stretch tests conducted at low and high strain rates (up to 500%/s): 432 MPa hoop yield stress ($\sigma_{\theta Y}$) and 516 MPa hoop ultimate tensile stress ($\sigma_{\theta UTS}$), both at RT (22°C). On the basis of unpublished ANL data, the axial tensile properties measured at RT and 0.1%/s strain rate were: 400 MPa for σ_{xY} and 530 MPa for σ_{xUTS}. Although the strain-rate dependence of these properties should be relatively low, it is surprising that the literature values are treated as strain-rate independent. Use of these properties in the FEA model resulted in an under-prediction of load in the elastic-plastic displacement regime. Thus, plastic stresses vs. strains were modified during each ABAQUS run until a good fit was obtained to the RCT load-displacement data. The best fit was obtained with 540 MPa for $\sigma_{\theta Y}$ and 513 MPa for σ_{xY}, based on 5% anisotropy in these directions. The yield stress in the radial direction was set to 567 MPa. Given the number of variables involved in this problem, the best-fit solution is not unique. However, it is useful for illustrating the hoop stress distribution around the cladding wall as a function of ring displacement.

Figure 15 shows benchmark RCT results for an 8-mm-long, 17×17 M5® ring displaced to 0.7-mm at RT and at a displacement rate of 0.05 mm/s. The cladding outer diameter was 9.50 mm and the wall thickness was 0.57 mm. The best fit to the load-displacement curve was obtained with a hoop yield stress (at 0.2% offset) of 540 MPa.

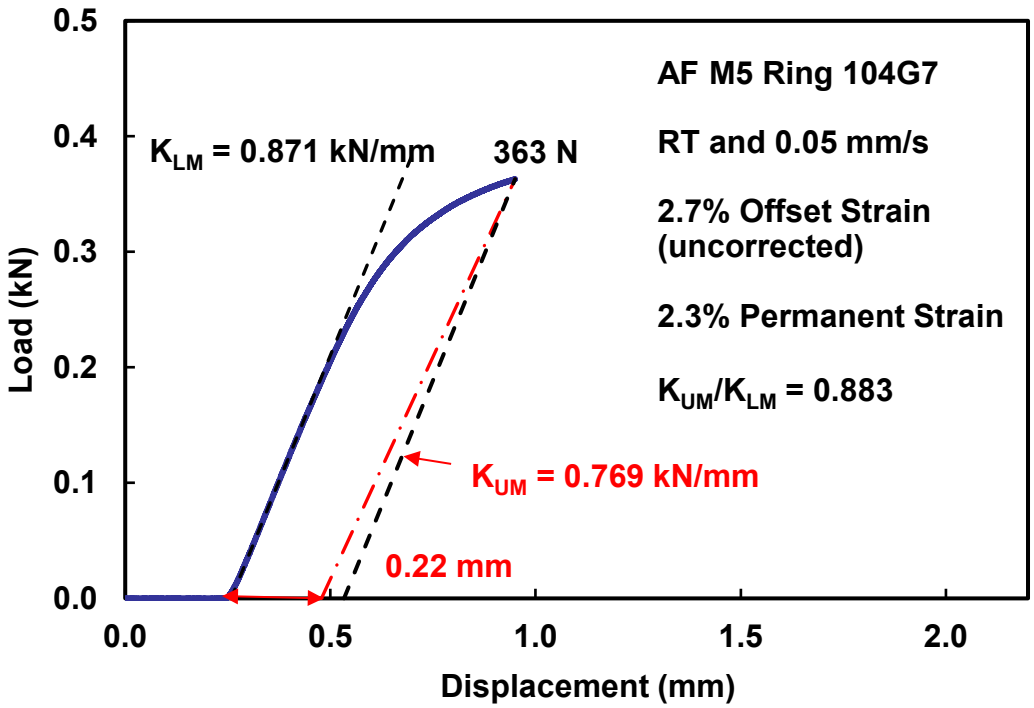

Figure 15: Load-displacement curve for an as-fabricated 17×17 M5® ring displaced to 0.7 mm at RT and 0.05 mm/s.

As shown in Fig. 16, the RCT is modeled by two rigid plates, one supplying the load (top) and the other acting as the support (bottom). The plates are attached to springs (not shown) representing the machine

stiffness. The coefficient of friction between the ring and the load/support plates was set to 0.1. Initially, there is loading only along the top outer diameter line. As displacement of the top plate increases, the contact area increases causing the line load to transition to a distributed load. In the elastic-displacement regime, the transition from line load to distributed load results in a slight increase in ring stiffness. Two cases were modeled: (a) elastic displacement up to 0.16-mm sample displacement and (b) elastic-plastic displacement up to 0.7-mm sample displacement. For the elastic case, numerous runs were conducted for rings with different length to determine the function f(v) described in Section 2.2. The ratio L/h_m was varied from 5 to 23, which corresponded to L values from 3 to 13 mm. Results are plotted in Fig. 17 for f(v) vs. L/h_m.

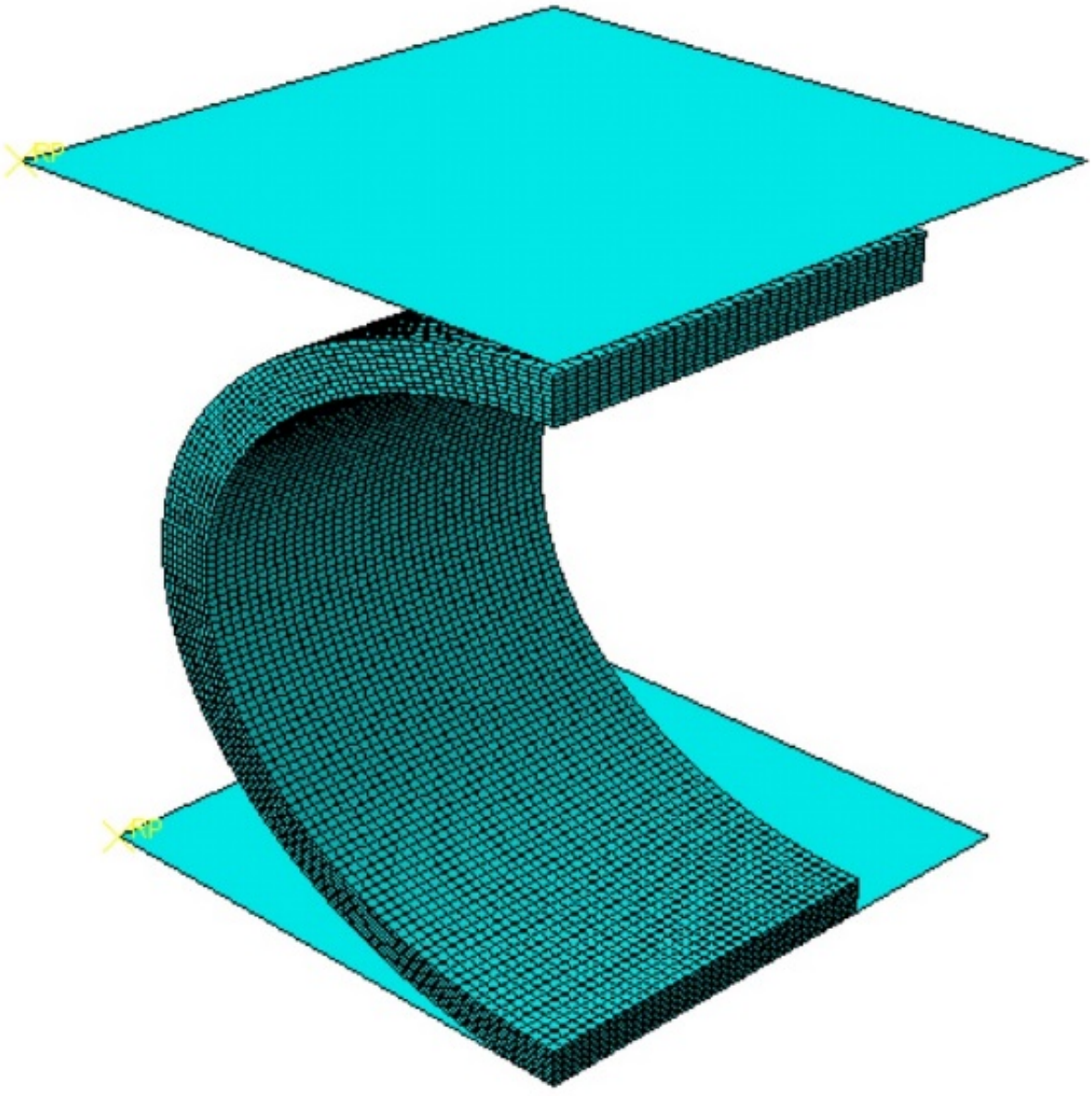

Figure 16: ABAQUS model for determining load vs. displacement, stress and strain in the RCT.

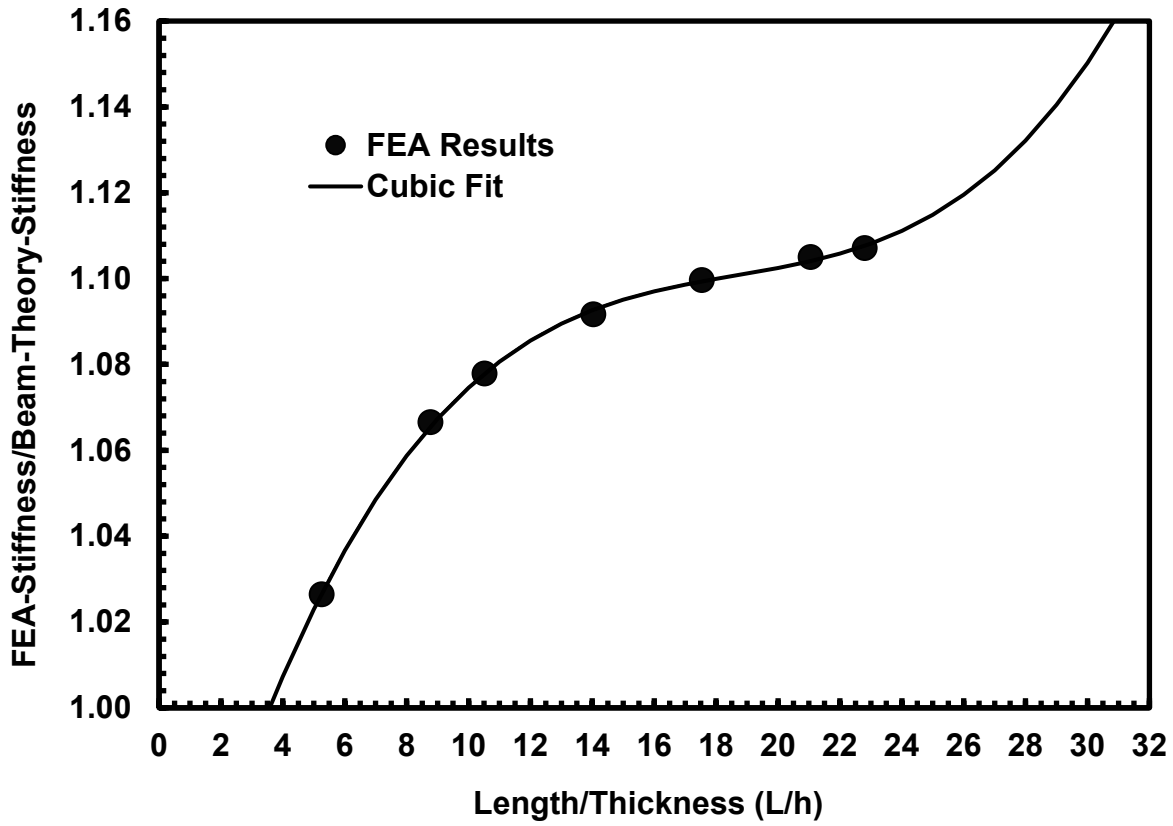

Figure 17: Plot of f(v) vs. the length to thickness ratio, where f(v) = the FEA-calculated ring stiffness divided by normal beam-theory (f[v] = 1) stiffness.

The cubic fit was chosen for interpolation between the FEA-calculated points shown in Fig. 17. Caution should be exercised in using the following correlation for L/h ratios >26:

$$f(v) = 0.922 + 0.02632\ (L/h) - 1.347\times10^{-3}\ (L/h)^2 + 2.411\times10^{-5}\ (L/h)^3 \qquad (4)$$

Figure 18 shows the distribution of elastic hoop stresses around the ring. The largest tensile hoop stresses are concentrated in the region around the 12 and 6 o'clock inner surfaces. Tensile hoop stresses, which are ≈40% less, are also concentrated around 3 (not shown) and 9 o'clock outer surfaces.

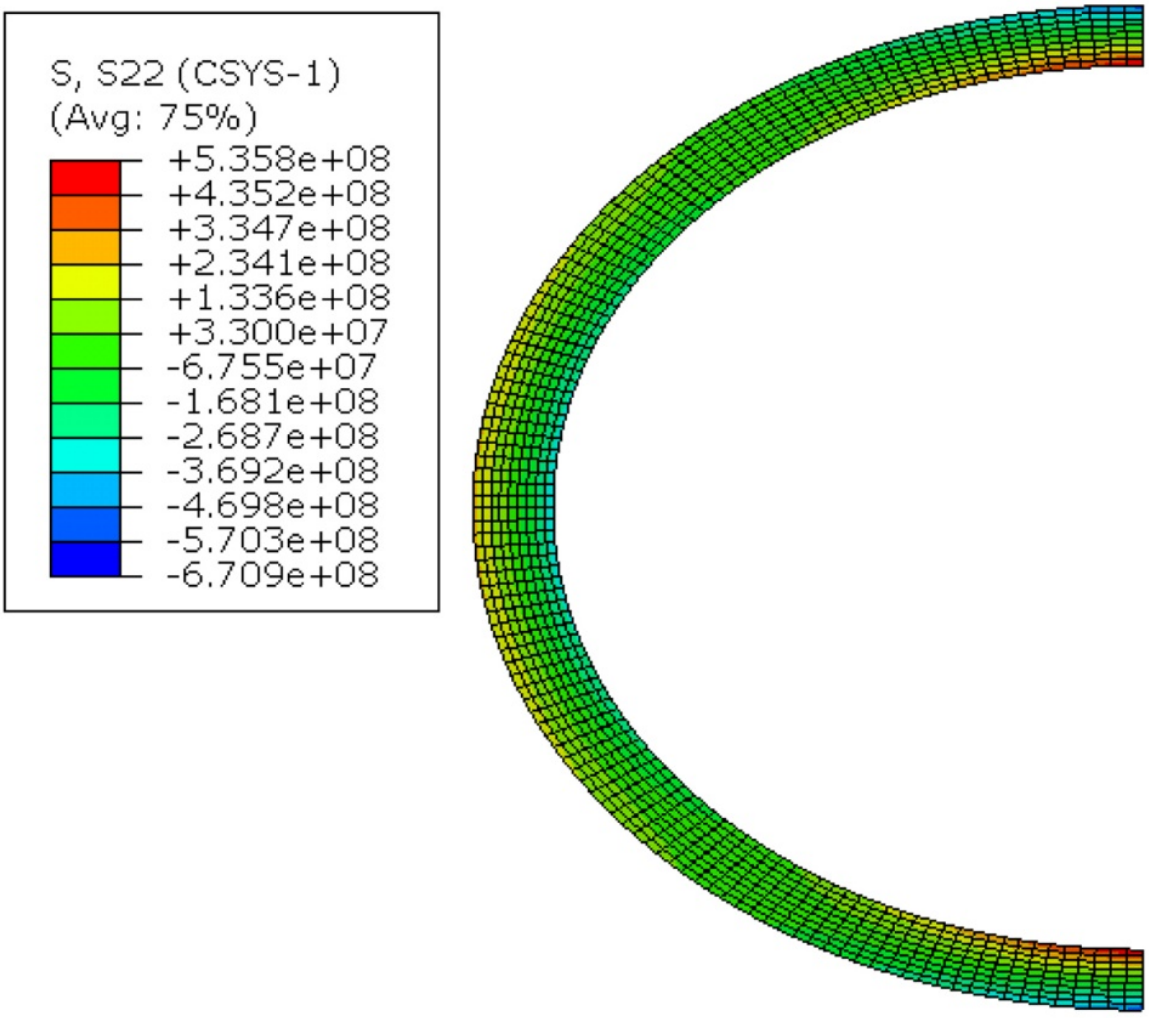

Figure 18: Elastic hoop stress distribution for an 8-mm-long (9.50-mm OD and 0.57-mm wall) M5® ring subjected to 0.16-mm displacement at RT and 0.05 mm/s.

The results are significant for the understanding of ring orientation with respect to the loading direction. For as-irradiated HBU-fuel Zry-4 and ZIRLO™ rings with relatively thick hydride rims and only circumferential hydrides, rings should be oriented with the thickest hydride rim close to the 3 or 9 o'clock orientation. This is relatively easy to do because circumferential hydrides are continuous along the length of the ring and the hydride-rim thickness, which varies with θ, does not vary along the length of the ring. For HBU-fuel M5™ (<120 wppm C_H), subjected to RHT, long radial hydrides precipitate near or at both the inner cladding surface, as well as within the cladding. Although an attempt can be made based on MET of a mid-span surface to position the ring accordingly, these radial hydrides are not continuous in length or orientation along the length of the ring. For RHT Zry-4 and ZIRLO™, the radial hydrides, although still discontinuous in the axial direction, exhibit "less discontinuity" due to the higher level of dissolved hydrogen available for precipitation. An attempt should be made to position the ring such that the longest radial hydrides emanating from the cladding inner surface are located at the 6 or 12 o'clock orientation. If the longest radial hydrides emanating from the cladding inner surface were

located in the low hoop stress regions (green in Fig. 18), it is unlikely from a stress perspective that cracking would occur along these rings.

Figure 19 shows the elastic-plastic stress distribution around the cladding wall for the ring displaced 0.7 mm (Fig. 15 case). If cracking does not occur at lower displacements, these results show the spread of plastic flow (stress magnitude > 540 MPa) with the increase in displacement from 0.16 mm to 0.70 mm.

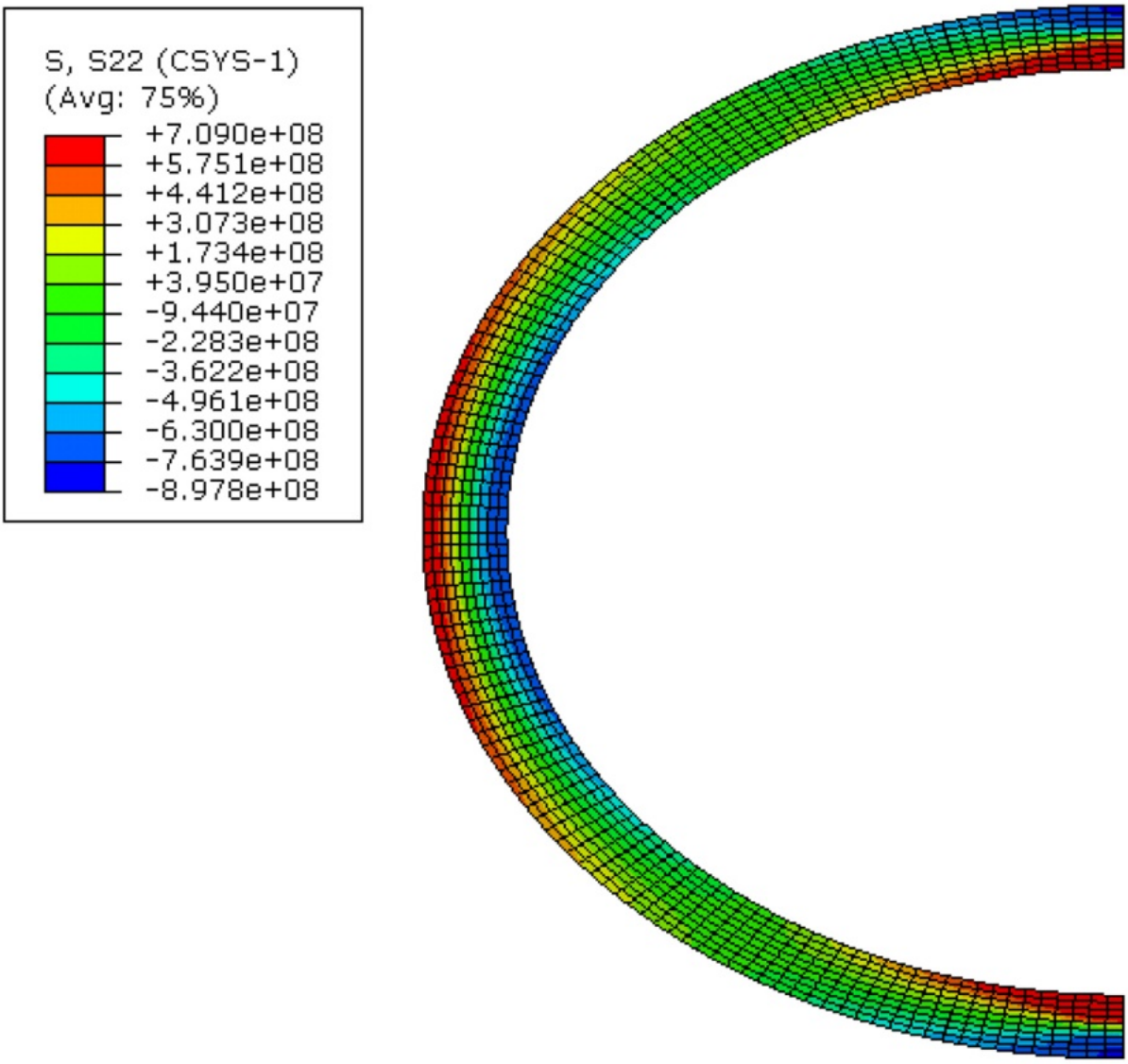

Figure 19: Elastic-plastic hoop stress distribution for an 8-mm-long (9.50-mm OD and 0.57-mm wall) M5® ring subjected to 0.7-mm displacement at RT and 0.05 mm/s.

Page intentionally blank

4. DUCTILITY DATA TRENDS FOR HBU-FUEL ZIRLO™ CLADDING

The material presented in this section is summarized in Ref. 17. However, it is repeated here, along with more details, because the figures in the double-column format of Ref. 17 were relatively small.

All load-displacement curves generated for HBU-fuel ZIRLO™ (since 2010) were reanalyzed using the improved correlation for determining the unloading slope (Eqs. 3a and 3b) and the implicit load-drop criterion illustrated in Figs. 13 and 14. While both tend to reduce ductility, there were several cases for which the implicit load-drop criterion had a significant effect on reducing ductility (i.e., offset strain prior to >50% wall cracking). Some samples previously classified as ductile were reassessed to be brittle.

The test materials and conditions listed in Table 1 were divided into three categories: high ductility (top row), medium ductility (middle row) and low ductility (bottom row). For as-irradiated cladding samples, the rings were ductile (6±1%) at RT independent of hydrogen content (350–650 wppm) and there was no evidence of a ductility transformation temperature at test temperatures ≥RT. The same conclusions applied to RHT samples for which the peak hoop stress was ≤80 MPa. Table 2 summarizes the RCT results for these high-ductility samples. The results are plotted in Fig. 20 along with a trend curve. The RHCF for these conditions is <10%. Yield and ultimate tensile strength decrease linearly with temperature and ductility increases with temperature. The hyperbolic tangent fit to the high-ductility data results from limiting the test to 1.7-mm displacement (≈10% offset strain at RT).

Table 2 Summary of HBU-fuel ZIRLO™ cladding materials, RHT hoop stresses, RCT conditions and ductility results for samples that exhibited high ductility.

ANL ID	C_H, wppm	RHCF, %	σ_θ (PCT), MPa	dδ/dt, mm/s	RCT T, °C	Offset Strain, %	Permanent Strain, %
646C	≈390±70	0	<70				
Ring 3				5	24	5.1	—
Ring 4				5	60	6.1	—
Ring 8				5	90	9.7	9.3
Ring 7				5	120	10.6	10.5
105A	530±70	0	0				
Ring 8				0.05	20	7.4	—
Ring 7				0.05	20	5.8	—
Ring 9				5	20	5.8	—
Ring 10				50	20	4.8	—
Ring 12				5	90	10.5	9.7
Ring 11				5	150	11.1	10.2
105B	535±50	9±4	80				
Ring 5		9±4		5	23	4.7	—
Ring 3		11±6		5	60	5.1	—
Ring 8				5	90	9.4	8.8
Ring 10				5	150	10.2	10.0
105G	≈650	0	0				
Ring 3				0.05	23	7.2	—
Ring 2				5	23	7.1	—
Ring 6				5	90	10.7	10.4
Ring 5				5	120	9.5	9.9

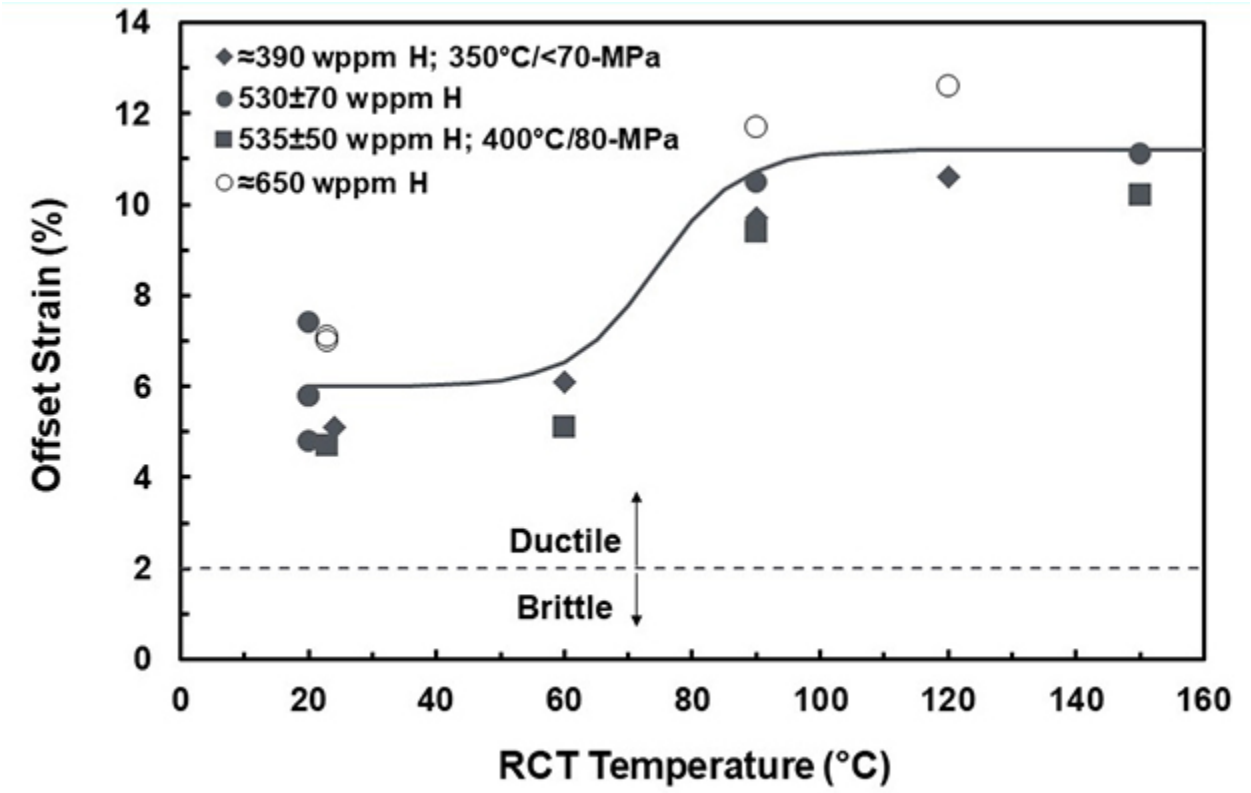

Figure 20: Ductility data and trend curve for high-ductility ZIRLO™.

Medium ductility samples and test conditions are those with ≈2% ductility at RT for which DTT <30°C. These include samples subjected to 350°C (646D) and 400°C (105C and 105D) peak RHT temperatures at peak hoop stresses in the range of 88±1 MPa. The RHCF for these samples is ≤20%. Table 3 summarizes ductility values and test conditions for these medium-ductility samples. The ductility data are plotted in Fig. 21, along with a hyperbolic tangent trend curve. Based on the trend line, the DTT is 26°C for the medium ductility samples. For 105C and 105D rings tested at 60°C, there was a high uncertainty regarding ductility determination due to the assessment of the implicit load drop. Although MET was performed for the 105D7 ring tested at 60°C, the sample was too severely cracked at multiple locations to allow understanding of what may have occurred between 0.6% offset strain and 4.0% offset strain. Figure 22 shows the load-displacement curves for the 105D7 ring tested at 60°C and the 105D4 ring tested at 26°C. The load-displacement curve for the ring tested at 26°C is straightforward to interpret. The load increases to 520 N at 2.2% offset strain prior to the 46% load drop and the subsequent steep load drop. Between these two load drops, the maximum load-carrying capability of the cracked ring is about 410 MPa. The 60°C ring begins minor load drops at 409 MPa, which is 23% lower than 520 N. The minimum load following the small load drops is 374 MPa, which is 29% lower than 520 N. Also, the load-carrying capability of the ring is about the same as the severely cracked ring tested at 26°C. These results suggest that severe cracking occurred at relatively low offset strain, but it is difficult to determine the point along the curve for which cracking was ≤50% of the cladding wall. In order to resolve this issue, the test would have to be rerun at a low enough displacement rate (e.g., 0.05 mm/s) to allow stoppage of the test at about 1% offset strain. A similar situation exists with the load displacement curve for 105C3 tested at 60°C, which had a 20% load drop at 1.4% offset strain (see Fig. 23). The peak load prior to the load drop was 467 N, as compared to 530 N at 1.8% offset strain for the 105C4 ring tested at 23°C.

Table 3 Summary of HBU-fuel ZIRLO™ cladding materials, RHT hoop stresses, RCT conditions and ductility results for samples that exhibited medium ductility.

ANL ID	C_H, wppm	RHCF, %	σ_θ (PCT) , MPa	dδ/dt, mm/s	RCT T, °C	Offset Strain, %	Permanent Strain, %
646D	387±72	16±9	87				
Ring 8				5	27	1.9	—
Ring 4		17±9		5	60	7.9	—
Ring 7		14±8		5	90	9.9	8.4
Ring 3				5	120	9.6	9.9
105D	480±131	18±7	88				
Ring 4		17±6		5	26	2.2	—
Ring 7				5	60	2.2±1.8	—
Ring 3				5	90	10.1	9.7
Ring 8				5	120	10.0	9.5
105C	530±115	19±9	89				
Ring 4				5	23	1.8	—
Ring 3		20±9		5	60	3.9±2.5	—
Ring 8		21±9		5	90	10.7	9.6
Ring 7				5	120	11.0	9.9

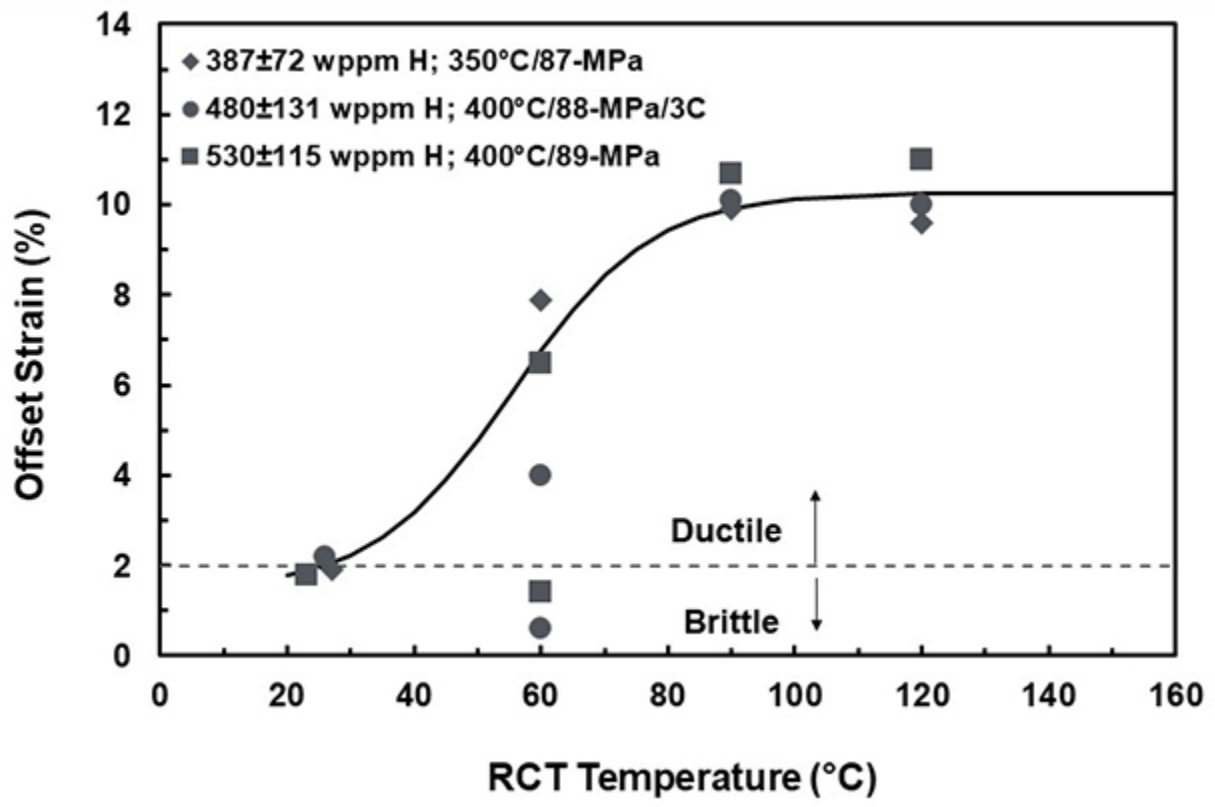

Figure 21: Ductility data and trend curve for medium-ductility ZIRLO™.

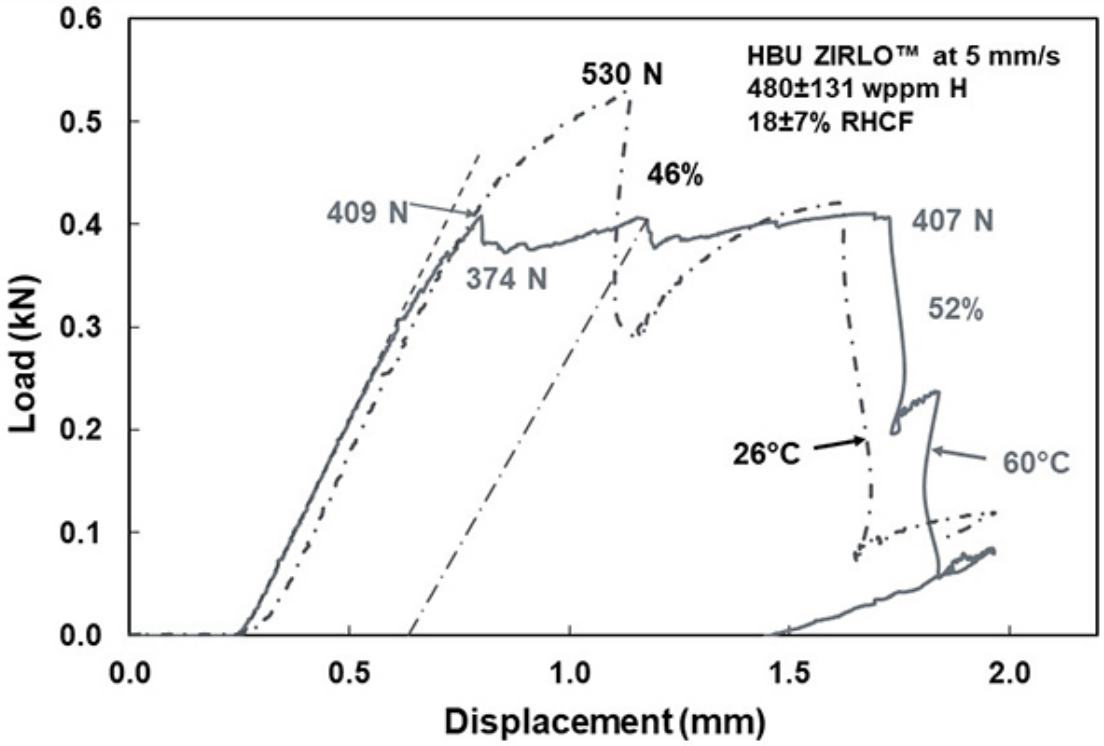

Figure 22: Load-displacement curves for 105D rings tested at 26°C and 60°C.

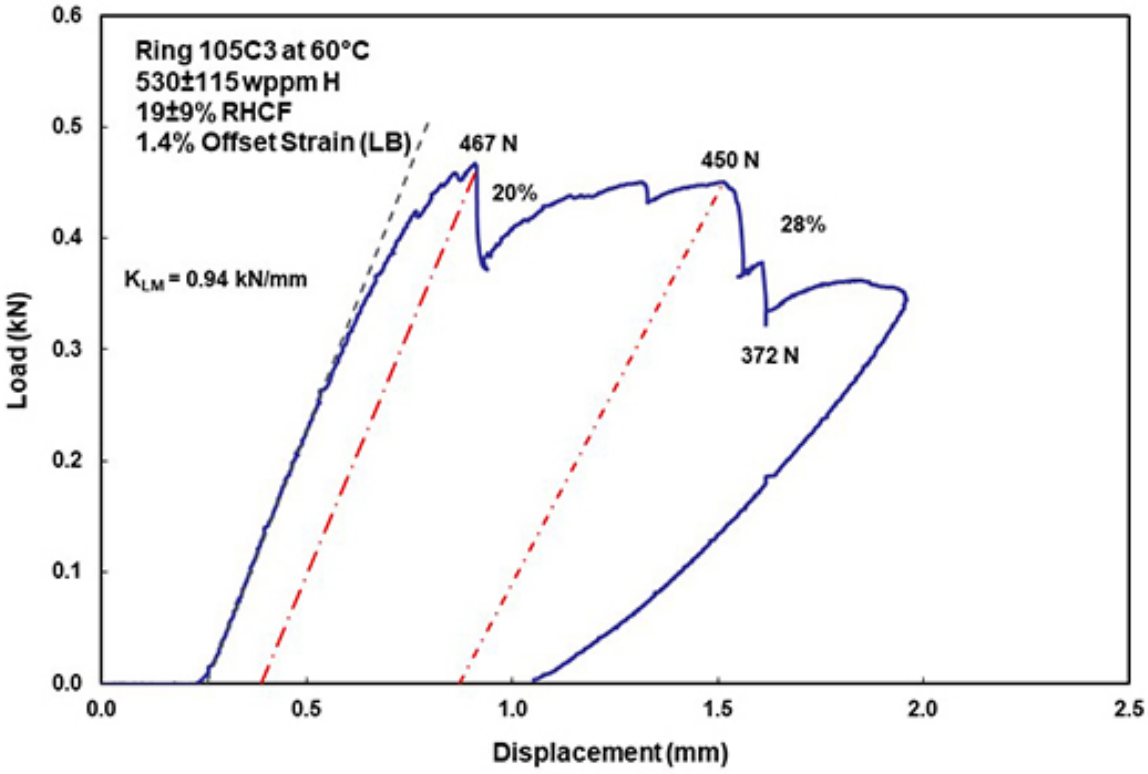

Figure 23: Load-displacement curves for 105C3 ring tested at 60°C.

Low ductility samples and test conditions are those with DTT >120°C. The peak RHT stress range for rodlets from which the rings were sectioned were in the range of 93 MPa to 111 MPa. These include samples subjected to 350°C (105E and 105F) and 400°C (648C and 648D) peak RHT temperatures. The RHCF for these samples is ≥27%. Table 4 summarizes the RHT peak hoop stresses, RCT test conditions and ductility values for these samples.

Table 4 Summary of HBU-fuel ZIRLO™ cladding materials, RHT hoop stresses, RCT conditions and ductility results for samples that exhibited low ductility.

ANL ID	C_H, wppm	RHCF, %	σ_θ (PCT), MPa	dδ/dt, mm/s	RCT T, °C	Offset Strain, %	Permanent Strain, %
105E	564±177	30±11	93				
Ring 4				5	90	0.7	—
Ring 7	569±148	26±10		5	120	1.1	—
Ring 3	568±200	37±8		5	135	9.1	9.8
Ring 8				5	150	8.2	—
105F	644±172	37±11	94				
Ring 8				5	120	0.7	—
Ring 3				5	135	1.0	—
Ring 4	625±199	37±12		5	150	6.2	—
Ring 7	664±176	38±13		5	150	0.8	—
648C	348±80	32±13	111				
Ring 5				5	30	0.3	—
Ring 3				5	90	0.4	—
Ring 10				5	120	1.4	—
Ring 8				5	150	10.0	9.4
648D	325±62	27±10	111				
Ring 3				5	30	0.6	—
Ring 8				5	150	8.2	—
Ring 10				5	150	9.2	—
Ring 5				5	150	8.8	—

Ductility data for the rings in Table 4 are plotted in Fig. 24. Data appear to be consistent for rings from rodlets 105E (93 MPa), 648C (111 MPa), and 648D (111 MPa). The trend curve is based on data points for these rings. However, data for 105F rings are consistently lower than data for the other cases. While not used to determine the trend curve, ductility values for 105F rings are plotted in Fig. 24. Given the similarities between 105E and 105F in terms of axial location along the fuel rod and peak RHT hoop stress, it is indeed surprising that radial hydrides appear to be longer in the 105F rings as compared to the 105E rings. There were two differences in RHT: (a) rodlet 105E was cycled three times (100°C drop per cycle) and slow cooling was maintained down to 200°C and (b) rodlet 105F was subjected to only one heating-cooling cycle, but slow cooling was maintained down to 130°C. Additional tests are needed with slow cooling maintained down to 130°C before conclusions can be drawn regarding this test parameter. Ductility values for rings from rodlets 105E and 105F decreased significantly relative to previously reported values due to the implied load drop criterion. This is shown for ring 105F7 tested at 150°C by comparing load vs. displacement with results from ring 105F3 tested at 135°C. Ring 105F7 never achieved the higher load recorded for 105F3 prior to the 13% load drop.

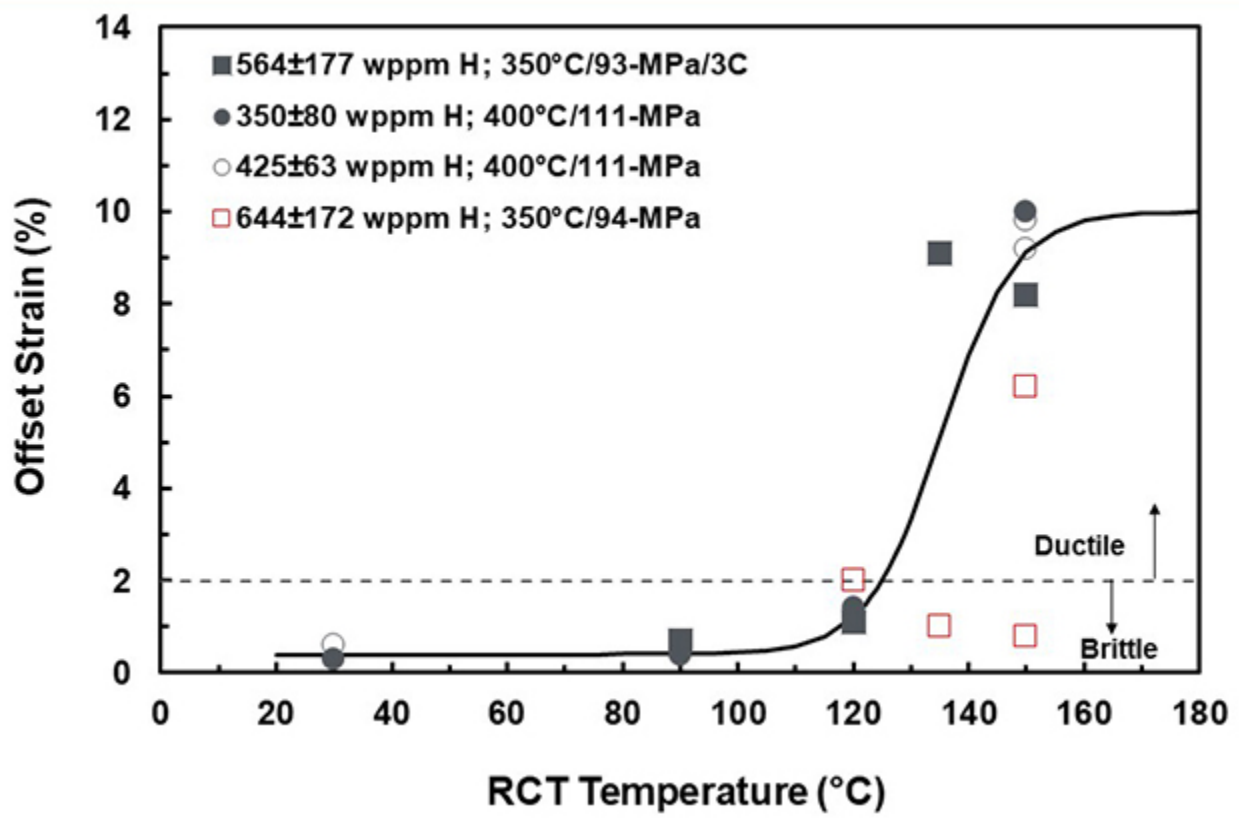

Figure 24: Ductility data and trend curve for low-ductility ZIRLO™.

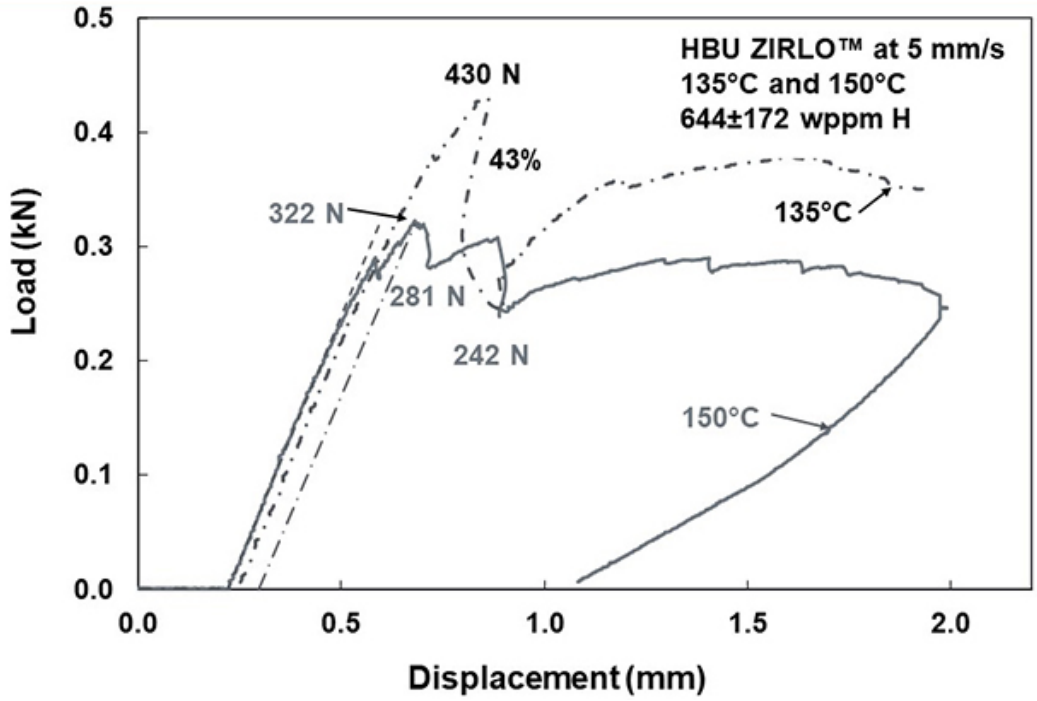

Figure 25: Load-displacement curves for 105F rings tested at 135°C (105F3) and 150°C (105F7).

It is important to confirm severe cracking (>50% of the wall thickness) for the implicit load-drop criterion. Figures 26−27 confirm the presence of long cracks at the 12 and 6 o'clock locations for the mid-span of ring 105F7. These cracks were also observed at one end of the ring.

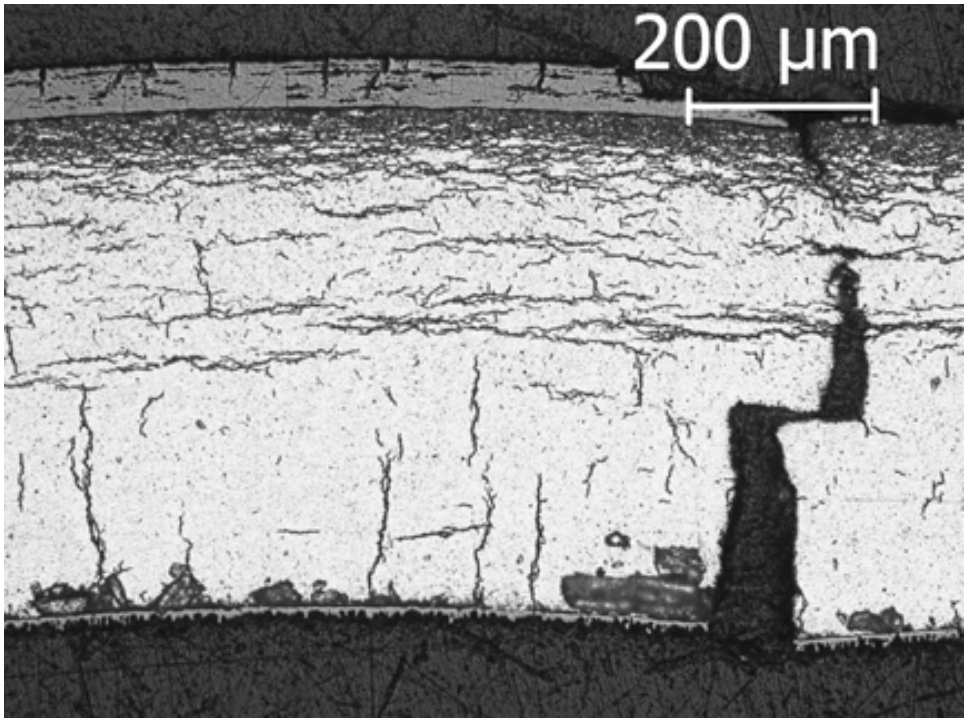

Figure 26: Long crack at the 12 o'clock location of ring 105F7 mid-span.

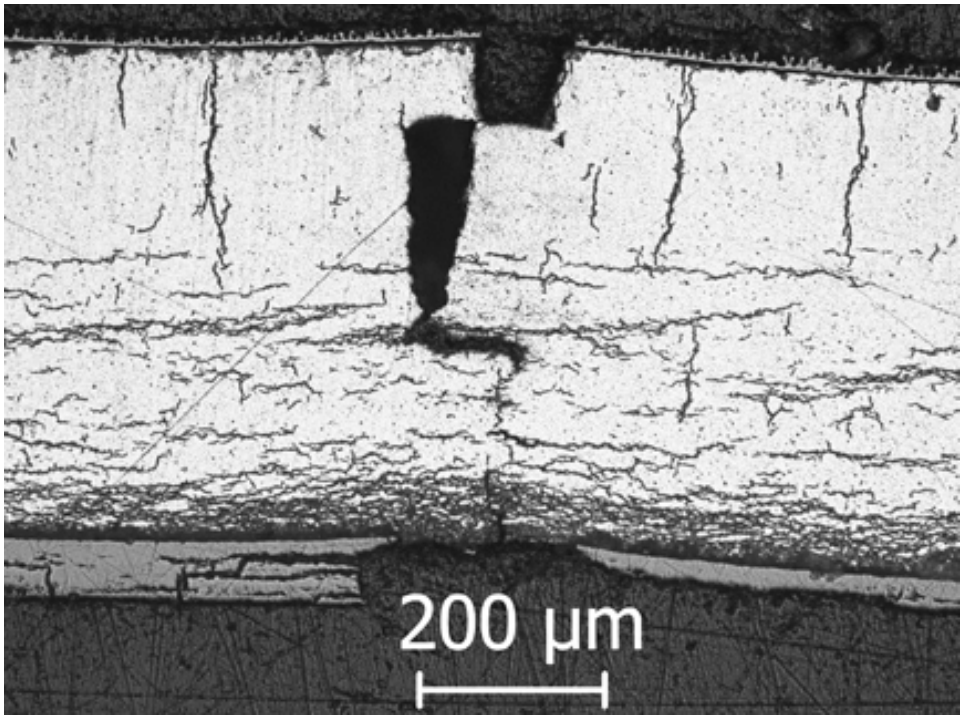

Figure 27: Long crack at the 6 o'clock location of ring 105F7 mid-span.

Page intentionally blank

5. RESULTS FROM CURRENT TEST WITH ZIRLO™

Rodlet 646B was subjected to RHT at 350°C PCT and 95 MPa peak hoop stress. The RHT temperature history is shown in Fig. 6. The sectioning diagram for 646B is shown in Fig. 28.

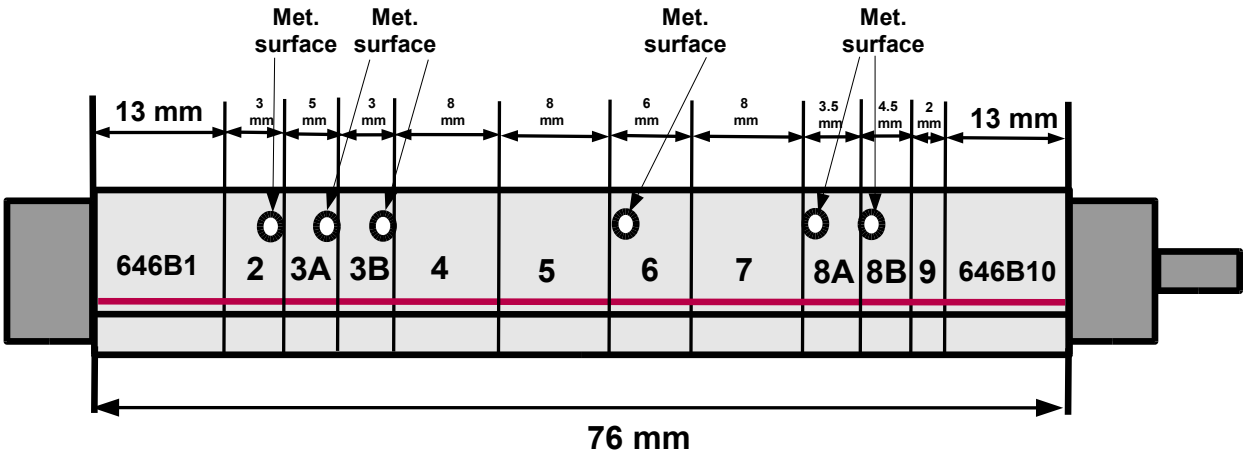

Figure 28: Sectioning diagram for rodlet 646B.

The indicated surface of ring 646B6 was used for MET. In the as-polished condition, 100X magnification images were taken at 12 equally spaced locations to determine the metal wall thickness. Images at 200X magnification were taken at locations within these 12 locations to determine oxide-layer thickness. Prior to sectioning, the outer diameter of the corroded cladding was measured to be 9.50 mm. The hydrogen content was estimated based on data for 646D and samples from segments of two other fuel rods with about the same oxide layer thickness. Rodlets 646B, 646C and 646D were fabricated from adjoining segments of the same fuel rod with 646B just below 646C. As shown in Table 5, the dimensions of these segments were comparable with the lowest segment having a slightly thinner oxide layer compared to 646C and 646D. The small difference in metal wall thickness was due to round off error (e.g., 0.554 mm vs. 0.556 mm).

Table 5 Characterization results for HBU-fuel ZIRLO™ rodlets 646B, 646C and 646D.

Parameter	Rodlet 646B	Rodlet 646C	Rodlet 646D
Outer Diameter (D_o), mm	9.50	9.50	9.49
Oxide Layer Thickness (h_{ox}), µm	27±1	30±1	30±1
Metal Outer Diameter (D_{mo}), mm	9.44	9.44	9.43
Metal Wall Thickness (h_m), mm	0.55	0.56	0.56
Metal Inner Diameter (D_{mi}), mm	8.33	8.31	8.31
Hydrogen Content (C_H), wppm	≈350±70	≈390±70	387±72

Following etching of the surface, about forty 100X magnification images were generated to visualize hydrides on the surface. These were overlapping images that covered the whole surface. The longer

radial hydrides in each of the 100X images were then imaged at 200X to determine continuity of these radial hydrides. On the basis of the longest radial hydride per 100X image, the average (± one standard deviation) RHCF was 26±8% and the maximum RHCF was 41%. Expectations were that the average RHCF would be about 30% with a maximum of about 50%. The surface was re-ground, re-polished and re-etched. Re-grinding removes about 0.1 mm of the surface. The imaging process was repeated, which resulted in 29±12% average RHCF and 53% maximum RHCF. Averaging these two sets of measurements results in 28±10% RHCF. The 28% average and 53% maximum were consistent with expectations for a rodlet subjected to 95-MPa hoop stress at 350°C. The longest radial hydride is shown in Figs. 29 (100X) and 30 (200X).

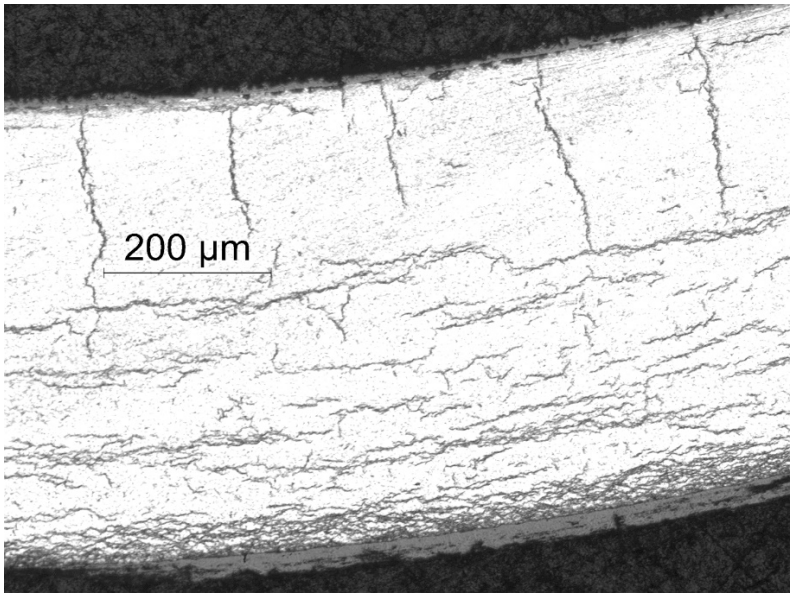

Figure 29: Longest radial hydride observed (at 100X) on the 646B6 surface.

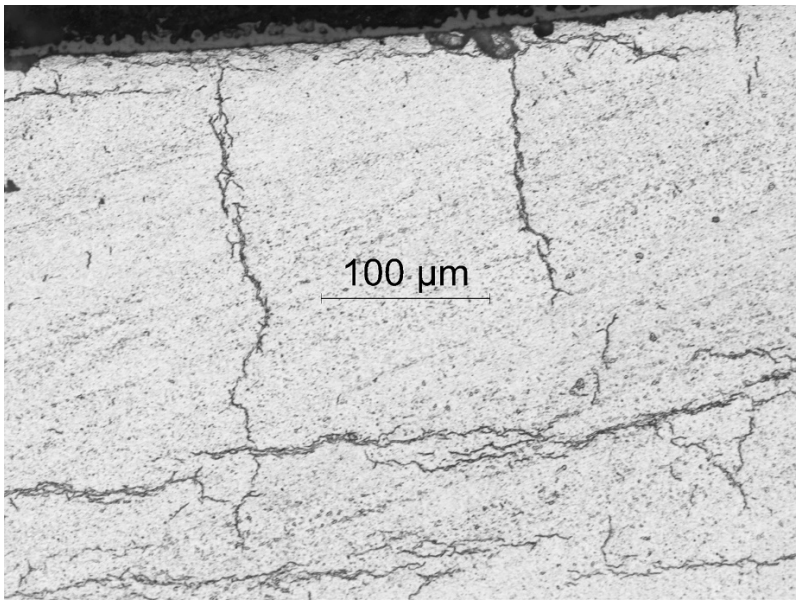

Figure 30: Longest radial hydride observed (at 200X) on the 646B6 surface.

RCTs were performed on all five rings (3, 4, 5, 7 and 8) shown in Fig. 28. The test sequence is important, as well as the axial location of the rings, for interpretation of results. Ring 646B5 (8.4-mm long) was tested first at 120°C because expectations based on data trends suggested that this ring would be brittle at this temperature. Figure 31 shows the load-displacement curve for ring 646B5. It rises to a peak load of 437 MPa at 0.9% offset strain prior to a 38% load drop. The criterion used was >25% load drop indicating a crack >50% of the wall thickness. The offset strain was determined by unloading at 437 MPa in accordance with the unloading slope given by Eq. 3a. As 0.9% is well below the 2% limit for ductility, the ring was assessed as brittle. The confidence in this result is high. Ring 646B7 (8.4-mm long) was tested next at 150°C and was expected to exhibit ductility based on data trends. Figure 32 shows the load-displacement curve for this ring. The load rose to 535 N at 3.5% offset strain prior to a 33% load drop. The offset strain was determined by unloading at 535 N in accordance with the unloading slope given by Eq. 3a. The confidence in this result is also high. Ring 646B4 (8.00-mm long) was tested at 100°C in order to generate another ductility data point that might be brittle, as well as to confirm the brittle behavior observed for the ring tested at 120°C. Load-displacement curves are shown in Figs. 33 (best estimate for offset strain) and Fig. 34 (upper bound for offset strain). Figure 33 shows the load rising to 370 N at 0.4% offset strain, dropping a small percentage, rising to 405 N at 2.4% offset strain and dropping 21%. The implicit load criterion was used to determine that unloading should occur at 370 N for a best estimate of ductility. The justification for this will become clearer after the results for ring 646B3 are presented. Figure 34 shows the 2.4% offset strain obtained by unloading at 405 N. This result is considered to be an upper bound regarding offset strain. Given the two large load drops after the 21% load drop from 405 N, MET would not be useful in supporting the judgment used because the sample would have multiple long cracks that occurred at higher displacements. If the test were repeated on adjacent ring 646B3 at the slow displacement rate of 0.05 mm/s, the test could be stopped after the small load drop at 370 N to determine the radial extent of cracking.

The 4th test was conducted at 170°C using ring 646B8 (8.00-mm long) in order to generate results with a higher offset strain for determination of the DTT between 120°C (brittle) and 150°C (ductile). Figure 35 shows that the 170°C ring exhibited full ductility (about 9% offset and permanent strains). These results are credible, but the validity of this test needs to be demonstrated by mapping the RHCF at the ends and mid-span of this ring. Two issues associated with end rings closest to the welds are the extents of stress discontinuity and HAZ. The RHCF profile will indicate the extent of the stress discontinuity arising from the weld. Along the transition, the hoop stress increases from zero at the weld to 95 MPa a short distance from the weld. The HAZ is expected to be shorter at the top of the rodlet because a successful weld was achieved after one try (two turns of the 1-mm-long electrode) and the hollow insert provided less of a heat sink as compared to the bottom solid insert.

The 5th test was conducted with ring 646B3 (7.7-mm long) at 100°C and 0.05-mm/s with the intent of stopping the test after the first small load drop. However, the ring exhibited no load drops and full ductility: 10.4% offset strain and 9.3% permanent strain (see Fig. 36). The results were highly suspicious. Metallographic imaging to determine RHCF vs. axial location from the weld will be used to provide guidance on how far away the ring has to be from the solid end plug to avoid stress discontinuity and the HAZ. It took 20 attempts to achieve a successful weld with about 10 minutes cooling time between attempts. Figure 28 shows the axial locations of the surfaces to be examined. MET of ring 646B2 has been completed. Results showed short radial hydrides (i.e., <5% RHCF) with a possible decrease in hydrogen on the right end of ring 646B2, which is equivalent to the left end of ring 646B3. This indicates that the left end of ring 656B3 was within the region of stress discontinuity. The results in Fig. 36 are useful in estimating the peak load that ring 646B4 should have achieved prior to the first load drop.

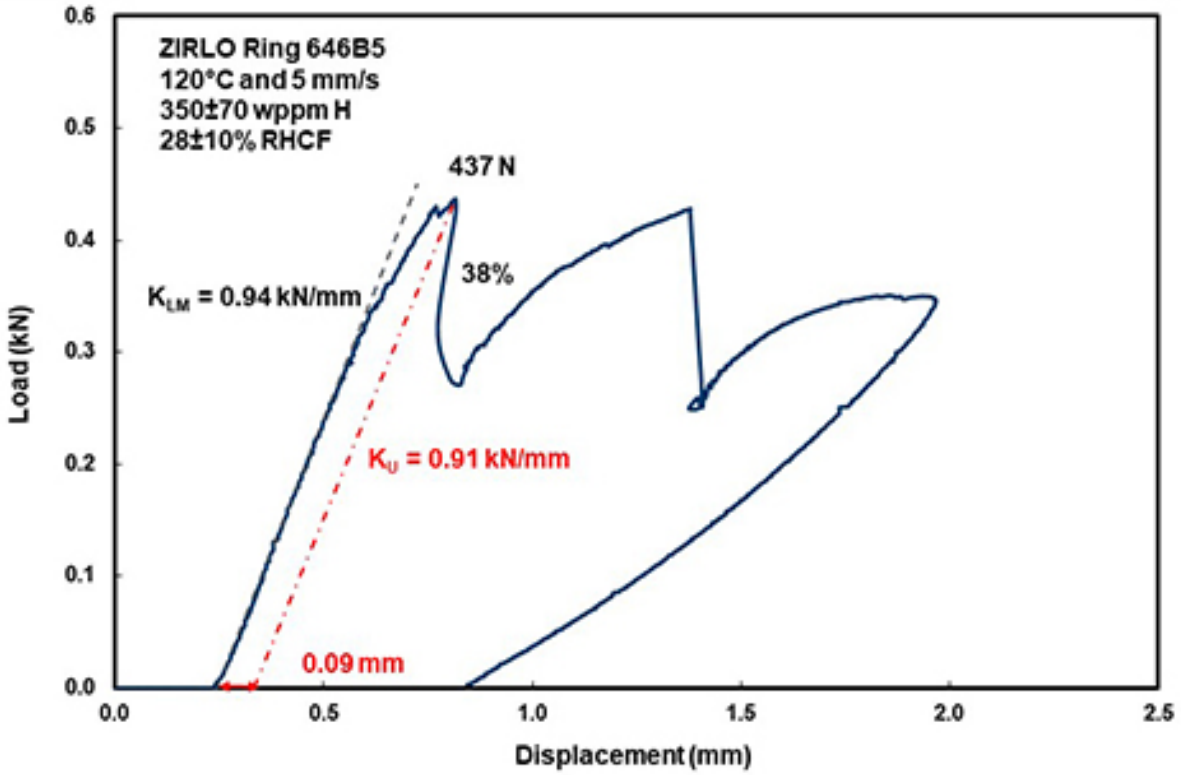

Figure 31: Load-displacement curve for ring 646B5 tested at 120°C and 5 mm/s.

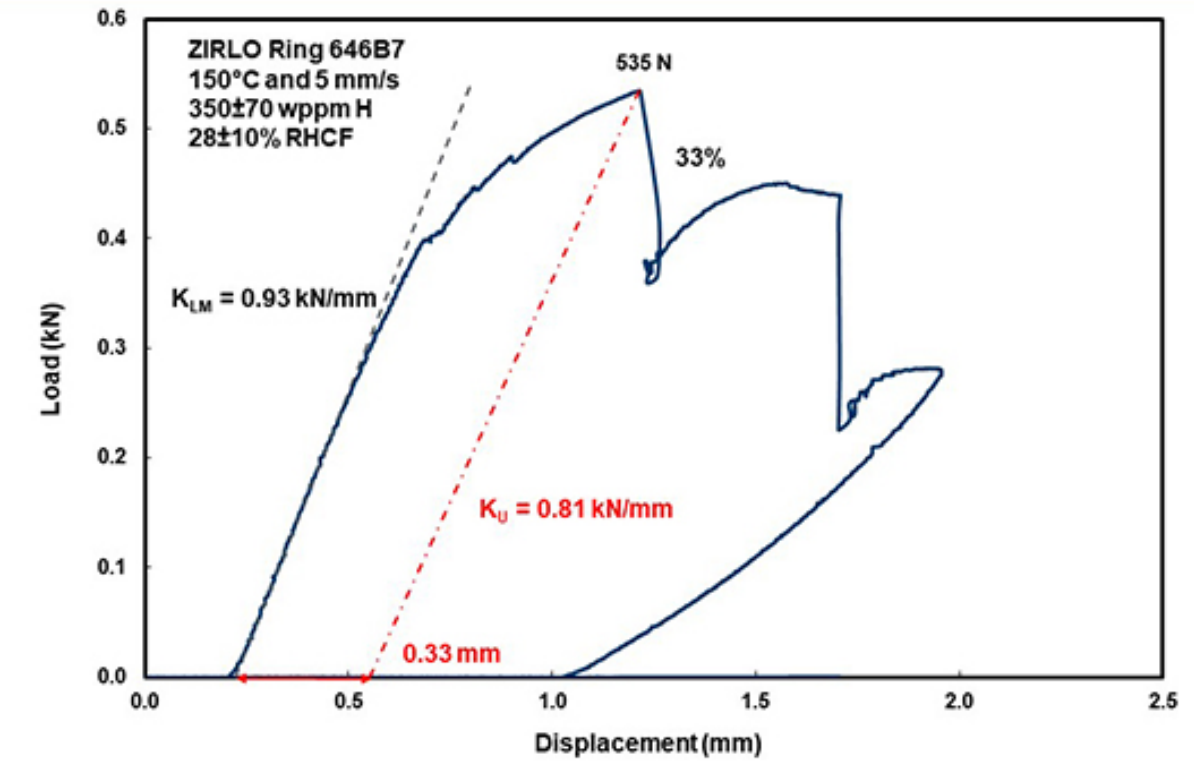

Figure 32: Load-displacement curve for ring 646B7 tested at 150°C and 5 mm/s.

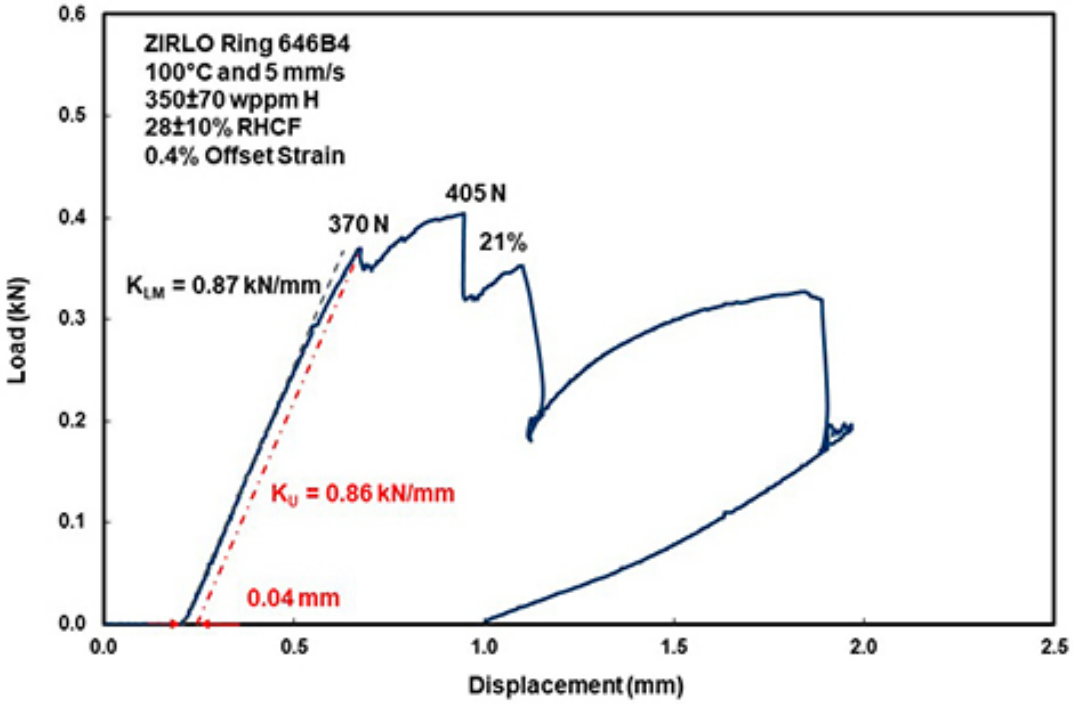

Figure 33: Load-displacement curve for ring 646B4 tested at 100°C and 5 mm/s. Best estimate for offset strain.

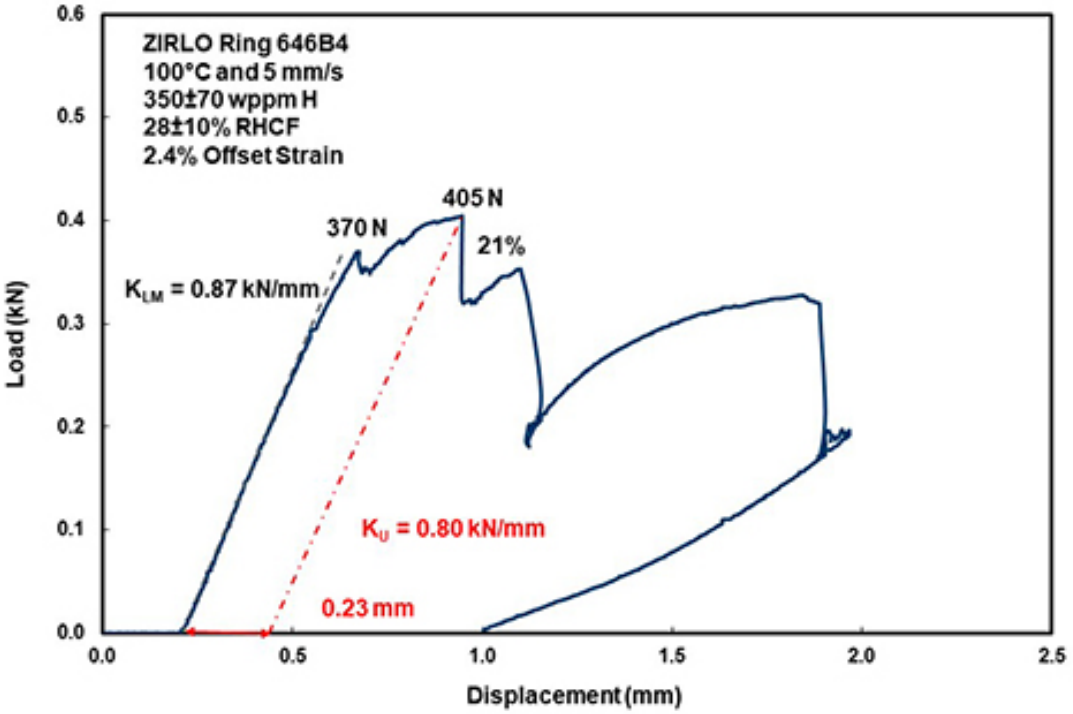

Figure 34: Load-displacement curve for ring 646B4 tested at 100°C and 5 mm/s. Upper-bound estimate for offset strain.

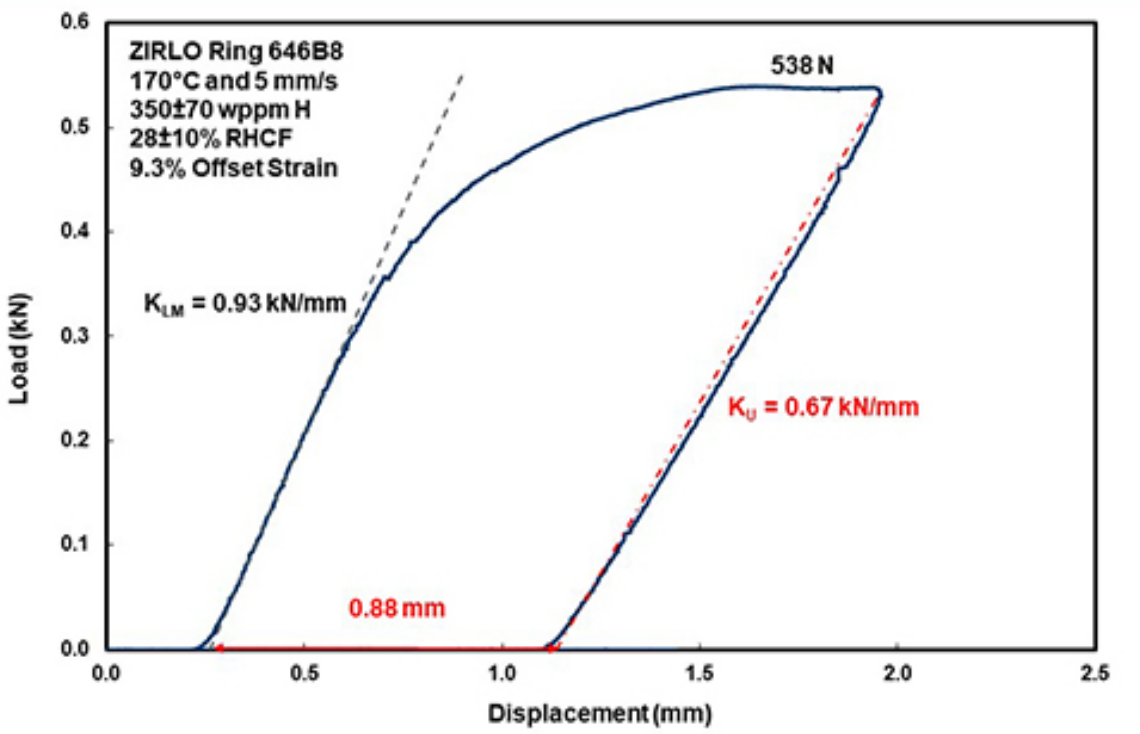

Figure 35: Load-displacement curve for ring 646B8 tested at 170°C and 5 mm/s.

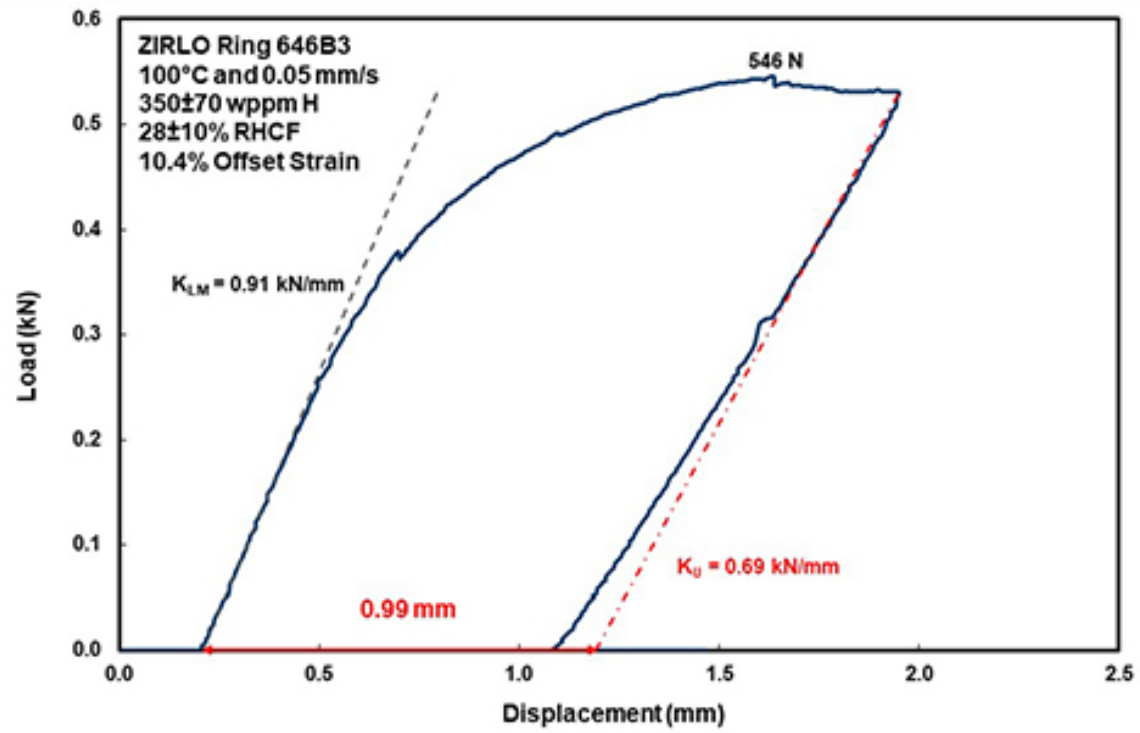

Figure 36: Load-displacement curve for ring 646B3 tested at 100°C and 0.05 mm/s.

6. DISCUSSION AND SUMMARY

Precipitation of Hydrides

Figure 1 shows dissolution and precipitation curves for cladding alloys, including the 65°C temperature drop before new hydrides will precipitate. The reason that a supersaturated solution of hydrides is needed to precipitate new hydrides is the density difference between the zirconium alloy (higher) and zirconium hydrides (lower). The density difference implies that precipitation of new hydrides requires the creation of a strain field such that the metal on either side of the hydride has to be displaced. However, it is not accurate to conclude that no hydrogen precipitates during the 65°C cooling. If circumferential hydrides remain at the PCT, the strain field from which partial dissolution of these circumferential hydrides also remains. Thus, some hydrogen will precipitate during cooling essentially in the same region from which it dissolved. At ≤65°C cooling from the PCT, there is a competition between the precipitation of new hydrides and growing of existing hydrides. For cooling under zero-stress conditions, hydrogen will tend to re-precipitate at locations from which it dissolved (memory effect). This includes regions in which radial hydrides may have been present prior to heating. As the hoop stress increases above a certain level, the strain field caused by the hoop stress favors precipitation of hydrides in the radial direction. Also, what appears to be a line of hydrides in optical microscopy images is actually a stack of hydride platelets oriented approximately normal to the "line" of the hydrides.

Circumferential hydrides are essentially continuous in the axial direction if the hydrogen content is high enough (e.g., >200 wppm). For as-irradiated cladding with sufficient hydrogen in the form of hydrides, cracks at the RCT 3 and 9 o'clock orientations can be observed at the ends and the mid-span of rings. Radial hydrides are not continuous in axial direction. However, for high enough hydrogen in the form of radial hydrides, the radial hydrides may have an "effective continuity" in terms of cracks induced by RCT loading. The amount of hydrogen available for precipitation depends on the amount of hydrogen in the starting material prior to heating and the PCT.

The Implicit Load-Drop Criterion

Previously, two criterion were used to determine the load-displacement point at which unloading should occur to calculate the offset strain. For highly brittle materials that crack during the elastic loading of the ring, >50% decrease in reloading slope implies >50% wall cracking and zero or near-zero offset strain. These results were confirmed experimentally and analytically using the FEA model for RCT samples [6]. This criterion was used for cladding samples with high RHT hoop stresses of about 140 MPa. For cladding rings that exhibit a smooth load vs. displacement curve prior to a load drop >25% (implies >50% wall crack), unloading should occur at the load prior to the load drop if that load is as high as expected based on test results for as-irradiated cladding and RHT cladding rings that crack at higher displacements. This result is empirical, but the FEA model could be used to confirm it. Most load-displacement curves generated in this program fall into this category. However, there are about a dozen load-displacement curves that exhibit small load drops near the end of elastic loading and at small displacements into the elastic-plastic regime. Post-test metallographic examinations have confirmed that multiple long cracks are present even if no significant load drop was observed. For these cases, it is important to compare the load carrying capability of the ring to the load carrying capability of as-irradiated rings or rings of similar geometry subjected to the same RHT. If the loads after minor load drops are significantly lower (e.g., >25% decrease), then significant cracking may have occurred during the transition from elastic to elastic-plastic displacement. This criterion is referred to as the implicit load-drop criterion. In the current work, all previously generated load-displacement curves were re-analyzed using all three criteria. It had

a significant effect on reducing the offset strain (i.e., ring structural ductility) prior to >50% wall crack for the cases in which the implicit load drop could be confirmed by comparison to sibling samples and by means of post-RCT metallographic imaging of the cracks. For other cases that could not be confirmed by means of metallographic examination (e.g., samples that exhibited large load drops at higher displacements and significant cracking), it is recommended in future testing that the test be repeated with another ring from the same rodlet at a slower displacement rate and the test be stopped at low displacement so that post-RCT imaging can confirm the existence of large cracks that may have formed under these conditions.

Ductility Data Trends for HBU-ZIRLO™ Cladding

RCTs have been conducted using rings from segments of as-irradiated cladding and rings from rodlets subjected to RHT at 350°C and 400°C PCT and peak hoop stresses in the range of 80−110 MPa. Other variables associated with RHT were: (a) single-cycle and multiple (3)-cycle heating and cooling and (b) controlled 5°C/h cooling down to 200°C vs. the current protocol of controlled cooling down to 130°C. Hydrogen contents of these segments and rodlets ranged from about 350 wppm to 650 wppm. Among all these variables, the peak cladding hoop stress during RHT appeared to have the greatest influence on the effective length of radial hydrides, ductility, and DTT. Data were separated into three general categories: (a) high ductility, (b) medium ductility, and (c) low ductility. High ductility conditions included as-irradiated cladding and RHT cladding subjected to ≤80 MPa peak hoop stress at 350°C and 400°C. Under these conditions, the RHCF was ≤10%, RT ductility was 6±1%, and no DTT was observed down to RT. Medium ductility samples included RHT cladding subjected to 88−89 MPa at 400°C and 87 MPa at 350°C. Under these conditions, the RHCF was ≤20% and the DTT was about RT. Low ductility samples include RHT samples subjected to 93-94 MPa at 350°C and 111 MPa at 400°C. The RHCF was ≥30±3%, the maximum RHCF was ≥50%, and the DTT was >120°C. The ductility data suggest a narrow stress range of 90±3 MPa during which the DTT increased by ≥100°C. The ductility data for the 350°C/94-MPa RHT rodlet (105F) was considerably lower than the ductility data for the 350°C/93-MPa 3-cycle RHT rodlet 105E. Correspondingly, the average RHCF for 105F was about 7% higher than for 105E. The higher hydrogen content (≈640 wppm) for 105F as compared to 105E (560 wppm) did not seem to play a role in these results. RCT samples from adjacent segment 105G with ≈650 wppm exhibited ductility values as high as those for as-irradiated ZIRLO™ with about 350 wppm. It remains unresolved why the RHCF was higher and the ductility values were lower for rodlet 105F.

The trend curves based on previous RCT data are plotted in Fig. 37 without data points except for 105F data, which are plotted because this test resulted in low ductility values relative to the data trend for RHT peak hoop stresses >90 MPa . The trend curves were useful in planning the test conducted recently, as well as planning one more test that should be conducted at 350°C PCT. In order to get a consistent database at 350°C, the two tests needed are: (a) ZIRLO™ at lower C_H (≈350 wppm) and about 94-MPa peak hoop stress and (b) ZIRLO™ at higher C_H (≈650 wppm) and about 86-MPa peak hoop stress. The rodlet currently tested had ≈350 wppm C_H and was subjected to RHT peak conditions of 350°C and 95-MPa hoop stress. The results were consistent with the low ductility data trends in that the average RHCF was 28%, the peak RHCF was 53%, the RCT samples were brittle at 100°C and 120°C and ductile at 150°C. The ring tested at 170°C retained full ductility of 9% with no evidence of cracking. Although the results are credible, the RHCF needs to be measured as explained in the following.

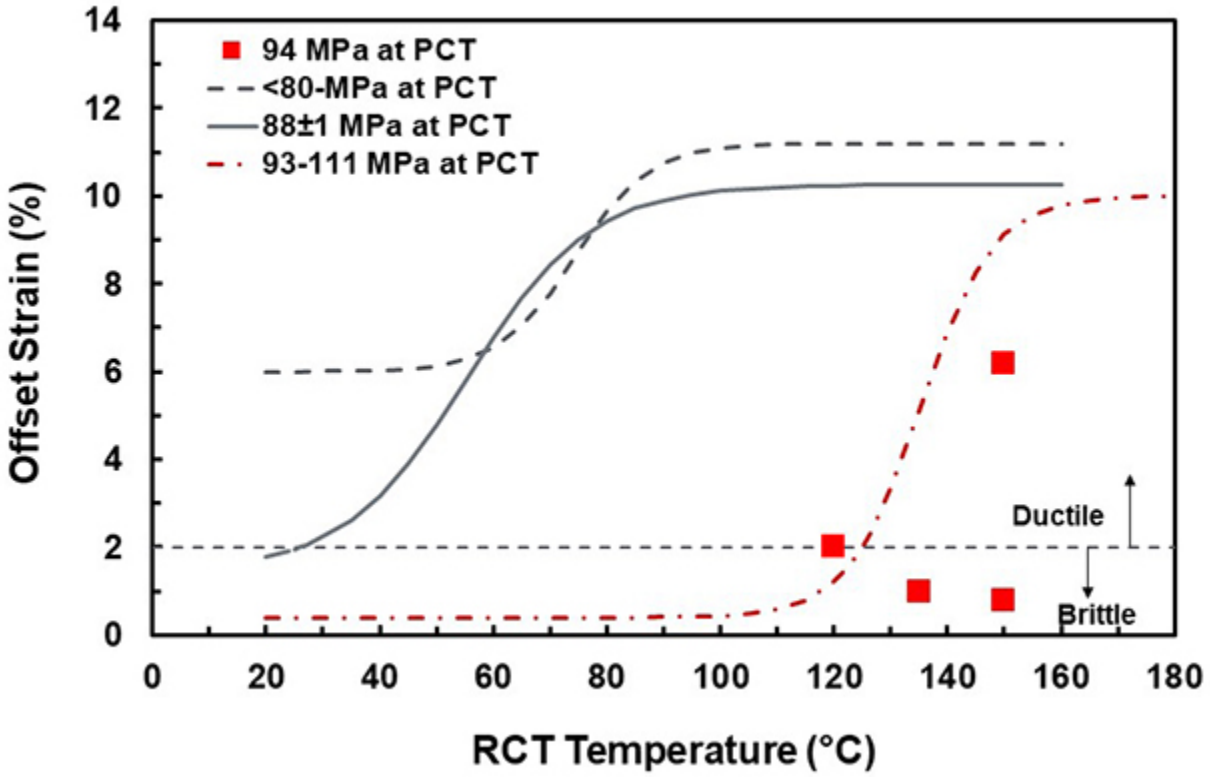

Figure 37: Ductility trend curves for HBU-fuel ZIRLO™ in the as-irradiated condition and following RHT (350°C and 400°C PCT) at the indicated peak RHT hoop stresses.

Rodlet End Effects

For the current test rodlet (646B), the length of the end-cap inserts was reduced from 15 mm to 10 mm, which allowed sectioning of an additional RCT sample. However, RCT results indicated that rodlet end effects were the major reason why the bottom ring (closest to the weld and the solid insert) exhibited unexpectedly high ductility at 100°C. Two end effects of concern are: (a) HAZ axial length and (b) hoop stress discontinuity axial length. In terms of the effective length of the HAZ for which partial annealing of radiation damage could occur, ring 646B3 was more susceptible to this effect because it took 10 attempts to achieve a successful weld and the 10-mm-long insert was solid, which provided a higher heat sink and required longer cooling times between attempts. Multiple weld attempts result in longer times at elevated temperature and even increases in temperature if the sample has not cooled down to low enough temperature between welding attempts. The top ring (646B8) required only one welding attempt to achieve a successful weld and the 10-mm insert was hollow. Partial annealing would be observed as a decrease in maximum RCT load. Work in progress includes the comparison of loads from RHT samples to the loads measured for as-irradiated cladding. Perhaps of more general concern is the axial length for cladding hoop stress to increase from 0 MPa at the weld interface to 95 MPa. The stress-discontinuity effect can be determined by measuring the RHCF as a function of axial distance from the weld. The work in progress includes measurements of the RHCF at the ends and the mid-span of both the top and bottom rings. Additional metallographic analyses will be performed for interior rings between the end rings to obtain a detailed profile of the RHCF as a function of distance from the bottom weld.

Effect of Peak RHT Hoop Stress on ZIRLO™ Cladding Ductility

Figure 37 suggests that the DTT for ZIRLO™ is highly sensitive to peak RHT hoop stresses in the narrow range of 90±3 MPa. However, the trend curve was obtained from samples with a wide range of hydrogen contents (350–650 wppm), with two different PCTs (400°C and 350°C), and with different RHT temperatures (200°C and 130°C) at which controlled 5°C/h cooling rate was terminated. The current data for rodlet 646B allows a direct comparison with previous data for rodlet 646D on the effects of peak RHT hoop stress for two segments from the same fuel rod (separated by only 80 mm along the fuel-rod axis). The cladding outer diameter, oxide layer thickness, wall thickness and hydrogen content values for both rodlets were comparable. Also, the RHT PCT was the same (350°C) for both rodlets, as was the controlled cooling from 350°C to 130°C. Figure 38 shows the ductility as a function of test temperature for rodlets 646D and 646B subjected to peak RHT hoop stresses of 87 MPa and 95 MPa, respectively. The 87-MPa RHT peak hoop rodlet (646D) exhibited a DTT of about 28°C, while the 95-MPa RHT peak hoop stress rodlet (646B) exhibited a DTT in the range of 138±5°C. Thus, the DTT increased by 110°C for this relatively small increase (8 MPa) in peak RHT hoop stress.

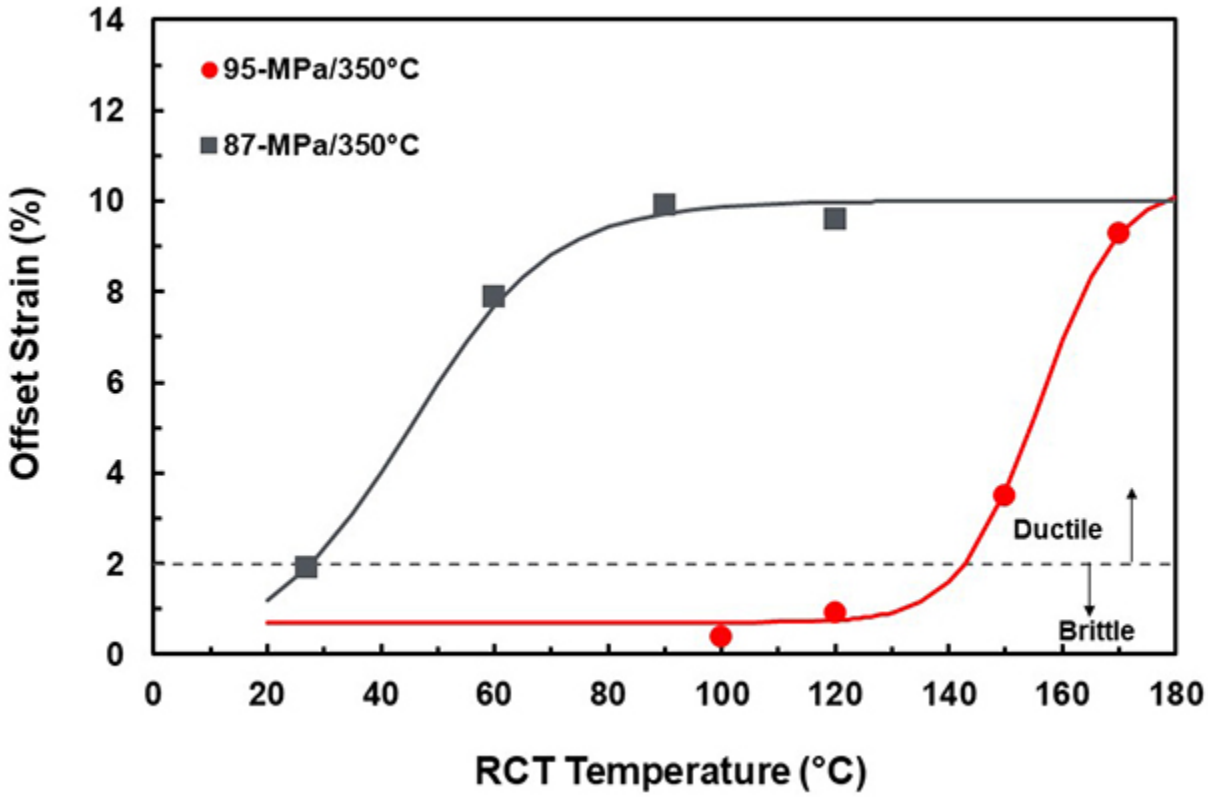

Figure 38: RCT ductility values for two similar ZIRLO™ rodlets for which the primary difference was the peak RHT hoop stress: 87 MPa and 95 MPa.

The 646B data point at 170°C requires validation, which consists of demonstrating that the RHCF values at the mid-span and ends of this ring are close to the 28% measured near the center of the rodlet. In other words, the validation consists of demonstrating that the ring tested at 170°C was free of end effects during welding and RHT. There is reasonable confidence that this ring, which was located near the top weld, was free of end effects because the insert was hollow (lower heat sink) and only one attempt (two turns of the weld head electrode) was needed to achieve a good weld.

Sister Rod Post-Irradiation Examinations (PIE) and Testing

The 25 sister rods include a wide range of linear heat ratings and cladding temperature gradients. In the Argonne study, a significant difference was observed between Zry-4 cladding from low-power fuel rods and ZIRLO™ cladding from high-power fuel rods. These differences may have had more to do with the differences in distribution of circumferential hydrides across the cladding wall than the differences in alloy compositions. Post-irradiation examinations (PIE) and testing of sister-rod cladding will resolve this issue. Reference 23 describes the PIE and testing planned for Phase 1 of the sister rod test program.

Page intentionally blank

REFERENCES

[1] Geelhood, K.J., W.G. Lusher, and C.E. Beyer, *PNNL Stress/Strain Correlation for Zircaloy*, Pacific Northwest National Laboratory Report PNNL-17700, July 2008.

[2] Geelhood, K.J., W.G. Lusher, and P.A. Raynaud, *Material Property Correlations: Comparison Between FRACAON-3.5, FRAPCON-1.5, and MATPRO*, NUREG/CR-7024, Rev. 1, October 31, 2014, ML14296A063.

[3] Nuclear Regulatory Commission, Interim Staff Guidance (ISG)-11, Revision 3, "Cladding Considerations for the Transportation and Storage of Spent Fuel," November 2003. ML033230335.

[4] Ahn, T., H. Akhavannik, G. Bjorkman, F.C. Chang, W. Reed, A., Rigato, D. Tang, R.D. Torres, B.H. White, and V. Wilson, *Dry Storage and Transportation of High Burnup Spent Nuclear Fuel*, NUREG-2224, July 2018 draft report for public comment.

[5] Billone, M.C., T.A. Burtseva, and Y. Yan, *Ductile-to-Brittle Transition Temperature for High-Burnup Zircaloy-4 and ZIRLO™ Cladding Alloys Exposed to Simulated Drying-Storage Conditions*, Argonne National Laboratory Report ANL-13/13, NRC ADAMS ML12181A238, Sept. 2012.

[6] Billone, M.C., T.A. Burtseva, and R.E. Einziger, "Ductile-to-Brittle Transition Temperature for High-Burnup Cladding Alloys Exposed to Simulated Drying-Storage Conditions," J. Nucl. Mater. **433**, 431–448 (2013).

[7] Billone, M.C., T.A. Burtseva, J.P. Dobrzynski, D.P. McGann, K. Byrne, Z. Han, and Y.Y. Liu, *Phase I Ring Compression Testing of High-Burnup Cladding*, FCRD-USED-2012-000039, Dec. 31, 2011.

[8] Billone, M.C., T.A. Burtseva, and Y.Y. Liu, *Baseline Studies for Ring Compression Testing of High-Burnup Fuel Cladding*, Argonne National Laboratory Report ANL-12/58, FCRD-USED-2013-000040, Nov. 23, 2012.

[9] Billone, M.C., T.A. Burtseva, and Y.Y. Liu, "Effects of Drying and Storage on High-Burnup Cladding Ductility," Proc. IHLRWMC, Albuquerque, NM, April 28–May 2, 2013, Paper 6973, 1106–1113 (2013).

[10] Billone, M.C., T.A. Burtseva, and Y.Y. Liu, "Baseline Properties and DBTT of High-Burnup PWR Cladding Alloys," Proc. PATRAM 2013, San Francisco, CA, August 18–23, 2013.

[11] Billone, M.C., T.A. Burtseva, Z. Han, and Y.Y. Liu, *Embrittlement and DBTT of High-Burnup PWR Fuel Cladding Alloys*, Argonne National Laboratory Report ANL-13/16, FCRD-UFD-2013-000401, Sept. 30, 2013.

[12] Billone, M.C., T.A. Burtseva, Z. Han, and Y.Y. Liu, *Effects of Multiple Drying Cycles on High-Burnup PWR Cladding Alloys*, Argonne National Laboratory Report ANL-14/11, FCRD-UFD-2014-000052, Sept. 26, 2014.

[13] Billone, M.C., T.A. Burtseva, and M.A. Martin-Rengel, *Effects of Lower Drying-Storage Temperatures on the DBTT of High-Burnup PWR Cladding*, Argonne National Laboratory Report ANL-15/21, FCRD-UFD-2015-000008, Aug. 28, 2015.

[14] Billone, M.C. and T.A. Burtseva, *Effects of Lower Drying-Storage Temperatures on the Ductility of High-Burnup PWR Cladding*, Argonne National Laboratory Report ANL-16/16, FCRD-UFD-2016-000065, Aug. 30, 2016.

[15] Billone, M.C. and T.A. Burtseva, *Effects of Radial Hydrides on PWR Cladding Ductility*, Argonne National Laboratory Report ANL-17/14, SFWD-SFWST-2017-000001, Sep. 13, 2017.

[16] Billone, M.C. and T.A. Burtseva, *Results of Ring Compression Results*, Argonne National Laboratory Report ANL-18/36, SFWD-SFWST-2018-000510, Sep. 28, 2018.

[17] Billone, M.C., "Ductility of High-Exposure ZIRLO™ Cladding following Drying and Storage", accepted as paper 27578 for publication in the proceedings of the International High-Level Radioactive Waste Management Conference, Knoxville, TN, April 14-18, 2019.

[18] Kearns, J.J., "Terminal Solubility and Partitioning of Hydrogen in the Alpha Phase of Zirconium, Zircaloy-2 and Zircaloy-4," J. Nucl. Mater. **22**, 292–303, 1967.

[19] Kammenzind, B.F., D.G. Franklin, H.R. Peters, and W.J. Duffin, "Hydrogen Pickup and Redistribution in Alpha-Annealed Zircaloy-4," *Zirconium in the Nuclear Industry: 11th Intl. Symp.*, ASTM STP 1295, E.R. Bradley and G.P. Sabol, Eds., ASTM, pp. 338–370, 1996.

[20] McMinn, A., E.C. Darby, and J.S. Schofield, "The Terminal Solid Solubility of Hydrogen in Zirconium Alloys, *Zirconium in the Nuclear Industry: 12th Intl. Symp.*, ASTM STP 1354, G.P. Sabol and G.D. Moan, Eds., ASTM, pp. 173–195, 2000.

[21] Tang, R. and X. Yang, "Dissolution and precipitation behaviors of hydrides in N18, Zry-4 and M5® alloys," Intl. J. Hydrogen Energy, **34** (2009) 7269−7274.

[22] Fourgeaud, S, J. Desquines, M. Pettit, C. Getrey and G. Sert, "Mechanical characteristics of fuel rod claddings in transport conditions," Packaging, Transport, Storage & Security of Radioactive Material, Vol 20, no. 2 (2009), pp 69-76.

[23] Saltzstein, Sylvia J., Mike Billone, Brady Hanson, and John Scaglione, "Visualization of the High-Burnup Spent Fuel Rod Phase 1 Test Plan: Technical Memo," SAND2018-8042 O, Jul. 18, 2018.